

On the Formation Mechanism of Banded Microstructures in Electron Beam Melted Ti-48Al-2Cr-2Nb
and the Design of Heat Treatments as Remedial Action

Original

On the Formation Mechanism of Banded Microstructures in Electron Beam Melted Ti-48Al-2Cr-2Nb and the Design of Heat Treatments as Remedial Action / Wartbichler, R.; Clemens, H.; Mayer, S.; Ghibaud, C.; Rizza, G.; Galati, M.; Iuliano, L.; Biamino, S.; Ugues, D.. - In: ADVANCED ENGINEERING MATERIALS. - ISSN 1527-2648. - ELETTRONICO. - 23:12(2021), p. 2101199. [10.1002/adem.202101199]

Availability:

This version is available at: 11583/2958016 since: 2022-10-03T16:34:47Z

Publisher:

John Wiley and Sons Inc

Published

DOI:10.1002/adem.202101199

Terms of use:

This article is made available under terms and conditions as specified in the corresponding bibliographic description in the repository

Publisher copyright

(Article begins on next page)

On the Formation Mechanism of Banded Microstructures in Electron Beam Melted Ti–48Al–2Cr–2Nb and the Design of Heat Treatments as Remedial Action

Reinhold Wartbichler,* Helmut Clemens, Svea Mayer, Cristian Ghibaudo, Giovanni Rizza, Manuela Galati, Luca Iuliano, Sara Biamino, and Daniele Ugues

The formation mechanism of banded microstructures of an electron beam melted engineering intermetallic Ti–48Al–2Cr–2Nb alloy, the solidification behavior, and the heat treatment response are investigated via a process parameter study. Scanning electron microscopy, hardness testing, X-ray diffraction, electron probe microanalysis, thermomechanical analysis, electron backscatter diffraction, heat treatments, as well as thermodynamic equilibrium calculation, and numerical simulation were performed. All specimens show near- γ microstructures with low amounts of α_2 and traces of β_0 . Fabrication with an increased energy input leads to an increased Al loss due to evaporation, a lower α -transus temperature, and to a higher hardness. Banded microstructures form due to abnormal grain growth toward the bottom of original melt pools, whereas α_2 in Al-depleted zones enables a Zener pinning of the γ -grain boundaries, leading to fine-grained areas. Via numerical simulation, it is shown that increasing the energy input leads to larger maximum temperatures and melt pool sizes, longer times in the liquid state, and more remelting events. Solidification happens via the α -phase and increasing the energy input leads to an alignment of $(111)_\gamma$ in building direction. Furthermore, banded microstructures respond heterogeneously to heat treatments. Heat treatment is introduced based on homogenization via phase transformation to obtain isotropic microstructures.


made their entrance into fields like the biomedical sector or the aeronautical industry, where their advantages in terms of reduced waste, lead times, costs, and stockpiles besides the possibility to integrate functions, design components with high geometrical complexity, and rapid responses to market demands are already at a certain maturity level.^[3] Furthermore, time to fly and buy to fly ratios are reduced considerably.^[4] During the last 10 years AM also came in contact with the intermetallic structural material class based on the γ -TiAl phase, namely: titanium aluminides. γ -TiAl-based alloys offer outstanding specific properties of strength and Young's modulus as well as creep resistance at an application temperature range from 600 to 800 °C, especially when compared to polycrystalline nickel alloys.^[5] When analyzing the specific modulus versus specific strength properties at room temperature (RT) TiAl alloys ($\rho \approx 3.9\text{--}4.2\text{ g cm}^{-3}$) are, in fact, second to only beryllium-based alloys.^[5] These properties make them attractive candidates to substitute heavy

Ni-based superalloys ($\rho \approx 8\text{--}8.5\text{ g cm}^{-3}$), where, depending on the component, switching to TiAl-based alloys offers weight savings ranging from 20% to 50% for components like casings, vanes, shrouds, or turbine blades.^[6,7] With the challenges of today regarding climate protection and sustainability increasing engine efficiency besides reducing CO₂, NO_x, and noise

1. Introduction

Since its development in the 1980s additive manufacturing (AM) emerged from application in rapid prototyping and tooling into direct production.^[1,2] Powder bed-based AM technologies such as laser powder bed fusion or electron beam melting (EBM)

R. Wartbichler, H. Clemens, S. Mayer
Department of Materials Science
Montanuniversität Leoben
Franz-Josef-Str. 18, 8700 Leoben, Austria
E-mail: reinhold.wartbichler@unileoben.ac.at

 The ORCID identification number(s) for the author(s) of this article can be found under <https://doi.org/10.1002/adem.202101199>.

© 2021 The Authors. Advanced Engineering Materials published by Wiley-VCH GmbH. This is an open access article under the terms of the Creative Commons Attribution-NonCommercial-NoDerivs License, which permits use and distribution in any medium, provided the original work is properly cited, the use is non-commercial and no modifications or adaptations are made.

DOI: 10.1002/adem.202101199

C. Ghibaudo, S. Biamino, D. Ugues
Department of Applied Science and Technology
Politecnico di Torino
Corso Duca degli Abruzzi 24, 10129 Torino, Italy

C. Ghibaudo, G. Rizza, M. Galati, L. Iuliano, S. Biamino, D. Ugues
Consorzio Interuniversitario Nazionale per la Scienza e Tecnologia dei Materiali (INSTM)
UdR Politecnico di Torino
Via Giuseppe Giusti 9, 50121 Firenze, Italy

G. Rizza, M. Galati, L. Iuliano
Department of Management and Production Engineering
Politecnico di Torino
Corso Duca degli Abruzzi 24, 10129 Torino, Italy

emission, as well as fuel consumption has become more important than ever.^[8–10] As such, weight reduction, especially in rotating components, is an important approach to reach ambitious technical engine specifications.^[11] Drawbacks in the usability of TiAl alloys came from their low ductility and difficult processing. Titanium aluminides remain sensitive to interstitial impurities deteriorating ductility significantly, especially when the interstitial content surpasses 0.1 mass% (m%).^[7] Furthermore, mechanical properties are highly dependent on the microstructure and the respective processing history, as well as composition sensitivity with regard to the Al content.^[6] Due to the high reactivity of TiAl melts cold wall crucibles were necessary for precision casting, which allowed only for low superheating, which in turn causes a number of casting problems, like incompletely filled molds and macro-porosity, making, subsequently, preheated molds a necessity, leading to slow cooling rates and coarse-grained microstructures with a high scatter in mechanical properties and pronounced segregation.^[12,13] The production of high-quality ingots is also challenging, but progress was made by increasing production volumes besides decreasing the costs considerably, for details the reader is referred to the following references.^[6,11] By overcoming many of these obstacles due to the combined efforts of research and development, TiAl alloys matured into application in commercial jet engine service. General electric announced the introduction of the cast Ti–48Al–2Cr–2Nb (in at% unless stated otherwise) alloy,^[14] into service as low-pressure turbine (LPT) blade material for the 6th and 7th stage of the LPT of the GEnX™ civil aircraft engine in 2006.^[15] The titanium aluminide alloy hereby was utilized to eliminate the cascading engine weight increase problem especially affecting rotating parts.^[16] Just recently Pratt and Whitney introduced the TNM alloy (Ti–43.5Al–4Nb–1Mo–0.1B) in the last LPT stage of the new geared turbofan engine, a novel process adapted 4th generation TiAl alloy exploiting the stabilization of the body-centered cubic (bcc) β -phase at elevated temperatures enabling forging with near-conventional methods by providing a sufficient number of independent slip systems.^[8,9,17] Still, development and application of titanium aluminide alloys remain exceedingly challenging, but the emerging EBM process appears to be well suited for TiAl alloys, and design freedom, as well as weight reduction, go hand in hand with the driving force for the TiAl alloy design. First of all, oxygen and nitrogen pickup is highly limited due to the vacuum environment (controlled vacuum of 10^{-3} mbar partial pressure of He) during EBM.^[18,19] In addition, the elevated processing temperature allows for titanium aluminides to be manufactured at building temperatures above their brittle-to-ductile transition temperature ($\approx 700^\circ\text{C}$)^[7] leading to crack-free components when manufactured with adequate processing parameters.^[3] Due to rapid solidification segregations are limited to small length scales, contrary to macroscopic segregations often witnessed in cast TiAl, so there is potential for the manufacture of larger products where segregations limit the homogeneity of the components and uniformity of properties must exist.^[12,20] Furthermore, the freedom of design allows for more complex geometries for turbine blades and other components with cooling channels or special lattice structures and the powder can be recycled, which complies with future sustainable use of limited resources.^[3,9,19,21] Mechanical properties of TiAl parts remain highly microstructure-sensitive,^[8] which makes

clarifying the processing-microstructure-property relationship a necessity. Several different additively manufactured TiAl alloys were already investigated, such as the aforementioned Ti–(47–48)Al–2Cr–2Nb alloy,^[3,21–42] or the TNM alloy,^[43–45] as well as high Nb bearing TiAl alloys.^[46–52] Many different microstructures of these various electron beams melted titanium aluminide alloys were reported, generally fine-grained. For the second generation alloy Ti–48Al–2Cr–2Nb (or Ti–47Al–2Cr–2Nb) the resulting microstructures after EBM are often described to have banded and/or heterogeneous regions, detailed as layered microstructures of duplex-like fine grains and coarser γ -grains^[27]; a duplex microstructure consisting of a coarse equiaxed γ -single-phase region and a fine two-phase region of γ and α_2 ^[37]; microstructures with fine equiaxed grains and some coarse grains appearing in bands parallel to the powder layers^[3,18,21,22]; a unique layered microstructure of duplex-like regions and equiaxed γ -grain layers, also called γ -bands^[25]; a bimodal microstructure separating fine and coarse-grained areas^[41]; or a microstructure without columnar grains but fine equiaxed regions of lamellar γ/α_2 -colonies and coarse γ -grains.^[32] Explanations for the formation of such microstructures include the evolvement of the microstructure as the result of the double cascading peritectic reaction (with α_2 and γ from the initial solidified melt and γ -grains as the result of the second peritectic reaction $\alpha + L \rightarrow \gamma$),^[37] the formation of coarse equiaxed γ -grains in bands as the result of local overheating,^[3,22] and a certain part of the duplex microstructure being subject to annealing just above the eutectoid temperature, transforming it into γ -bands.^[27] Unfortunately, these layered and/or banded microstructures show anisotropic mechanical properties when it comes to tensile and fatigue testing,^[25,27] which are often unacceptable for application. The knowledge of the processing-related formation mechanism of banded microstructures and the possible remedies is, therefore, necessary.

Furthermore, a common appendage of TiAl manufactured by EBM is the evaporation of volatile elements near the surface of the melt baths, such as Al with its high vapor pressure.^[34,36] Examples of quantified Al loss in the course of EBM for Ti–48Al–2Cr–2Nb include a loss of 2.3 at%,^[27] 0.5–4 at%,^[36] 3 at% with high energy input,^[30] 2 at%,^[25] below 2 m%,^[18] or even a loss of 7.37 at%,^[26] which might change the alloy constitution considerably and depends on process parameters. Such EBM parameters as the beam scan speed v [mm s^{-1}], the beam current I [mA], the acceleration voltage U [kV], and the line offset l_{off} [μm] can be conveniently combined into terms describing the general energy input such as the line energy E_L [J mm^{-1}] and the area energy E_A [J mm^{-2}], as expressed via Equation (1) and (2)

$$E_L = \frac{UI}{v} \quad (1)$$

$$E_A = \frac{UI}{vl_{\text{off}}} \quad (2)$$

Schwerdtfeger et al. observed an increase of the Al loss with an increased E_L as well as an increase of Al loss with increased I for constant E_L .^[36] It was concluded that lower beam currents lead to reduce overheating of the melt pool and, subsequently, a reduced Al loss. Klassen et al.,^[34] concluded that E_L controls the peak

temperature of the melt pool and, thus, the amount of Al evaporation as well as the ratio of melted to deposited material.

However, neither E_L nor E_A do, in fact, control the EBM process, but their constituents v , I , and I_{off} along with the beam strategy. With appropriate control of these process parameters, it is possible to control the melt pool's dimension, duration, and temperature and, thus, control the amount of evaporation, as the loss of Al gets reduced using less energetic process parameters.

Nevertheless, heterogeneous distributions of Al in consolidated TiAl samples remain a challenge, and an overarching attempt to study the formation mechanism of these banded microstructures, also taking into account the solidification mechanisms with respect to the process parameters and in connection with the process-related Al loss, is still lacking.

A part of the authors previously reported for an EBM TiAl alloy that the adjusted microstructure, apart from the very top, is best described by a long term intrinsic cyclic annealing in the course of the EBM process, which can be approximated by the thermodynamic equilibrium at building temperature, which was found to be $\approx 50^\circ\text{C}$ above the preheating temperature.^[43] As hour-long building at elevated temperature led to a considerable coarsening of the lamella spacing in γ/α_2 -colonies, the full-grain structure was easily resolvable with a conventional scanning electron microscope (SEM), revealing pronounced heterogeneous phase distributions as a result of the heterogeneous Al distribution after evaporation of the aforementioned chemical element.^[44] Hot isostatic pressing (HIP) and a subsequent heat treatment remain, therefore, mandatory for electron beam melted TiAl alloys.

Although heat treatment studies on electron beam melted TiAl were performed,^[3,18,21,22,37,38,42,45,46,51] no investigation of the heat treatment response with regard to the respective processing parameters, especially considering the tendency to form banded microstructures, has been undertaken yet to the authors' best knowledge.

In this context, this article addresses the formation mechanism of the banded/layered microstructure in EBM Ti–48Al–2Cr–2Nb by a process parameter study taking into account the changes in overall chemistry, microscopic elemental and phase distribution, mechanical properties, as well as solidification behavior. The claims made are supported by thermodynamic equilibrium calculations and numerical simulation. Furthermore, the response to specific heat treatments is presented as a function of the respective parameter set, and, finally, a heat treatment route as remedial action is introduced, which can be taken into account during future alloy design processes to tailor TiAl alloys toward an industrial-scale fabrication via EBM.

2. Microstructural Characterization

The chemical compositions of the investigated electron beam melted Ti–48Al–2Cr–2Nb alloy samples after EBM, as established by X-ray fluorescence spectroscopy (XRF) and carrier gas hot extraction (CGHE), are listed in **Table 1**. Information about the EBM process and the different manufacturing parameters of the five cubics ($30 \times 30 \times 30 \text{ mm}^3$) specimens can be found in Section 8. It becomes apparent that the overall chemical composition is a function of the manufacturing parameters, which can be attributed to the evaporation of volatile elements, such as Al, during the vacuum process, as throughout described in the following references.^[34,36] With increased energy input, expressed as higher E_L , the Al content decreased from 48.13 at % for sample A to 46.96 at% for sample E, with samples B, C, and D being situated in between with Al contents of 47.96, 47.69, and 47.30 at%, respectively. The respective E_L , which remains constant during the process due to the square melting areas of the samples, is inserted in the micrographs to make the comparison of specimens with a different process history easier for the reader. **Figure 1** shows the microstructures of the consolidated EBM Ti–48Al–2Cr–2Nb alloy, obtained by SEM in back-scattered electron (BSE) mode, where each sample was manufactured with a different set of processing parameters (see Section 8). The building direction Z is upwards. **Figure 1a** depicts the microstructure of specimen A, manufactured with E_L of 0.17 J mm^{-1} . The microstructural constituents are outlined in the enlarged figure inset. Three different phases are distinguishable, all of them ordered intermetallic phases.^[8] The tetragonal γ -TiAl phase (L1_0 crystal structure) appears dark in the BSE contrast due to its high Al content, and seizes the greatest share of the microstructure. The hexagonal α_2 -Ti₃Al phase with the D0_{19} crystal structure is intermediate grey due to its high content of Ti and appears in two different morphologies: globular and in form of lamellae in γ/α_2 -colonies, which is also outlined in the figure inset. The β_0 -TiAl phase with its bcc B2 crystal structure and high content of heavy β -stabilizing elements, such as Nb, appears bright in the BSE contrast, and is scarcely distributed in globular fashion. This microstructure is classified as a so-called near- γ microstructure, as the predominant part of the microstructure is the globular γ -phase.^[7] **Figure 1b–e** shows the respective microstructures for samples B, C, D, and E, manufactured with increasing line energies. In general, all of these microstructures fall into the category of near- γ microstructures, however, showing important differences in terms of microstructural homogeneity and grain size. As a consequence of different processing parameters, namely, an

Table 1. Overall chemical compositions of the investigated samples as established by XRF and CGHE, the porosity as measured by image analysis, the macroscopic hardness according to HV10, and the respective α -transus temperature $T_{\alpha\text{T}}$ as established with thermomechanical analysis (TMA).

Sample designation	Ti [at%]	Al [at%]	Cr [at%]	Nb [at%]	O [m ppm]	Porosity [%]	HV10	$T_{\alpha\text{T}}$ [$^\circ\text{C}$]
A	bal.	48.13	1.88	2.01	1000	0.85	221	1367
B	bal.	47.96	1.88	2.01	1000	0.24	225	1362
C	bal.	47.69	1.87	2.03	960	0.11	229	1356
D	bal.	47.30	1.88	2.03	930	0.08	234	1348
E	bal.	46.96	1.87	2.04	920	0.04	261	1342

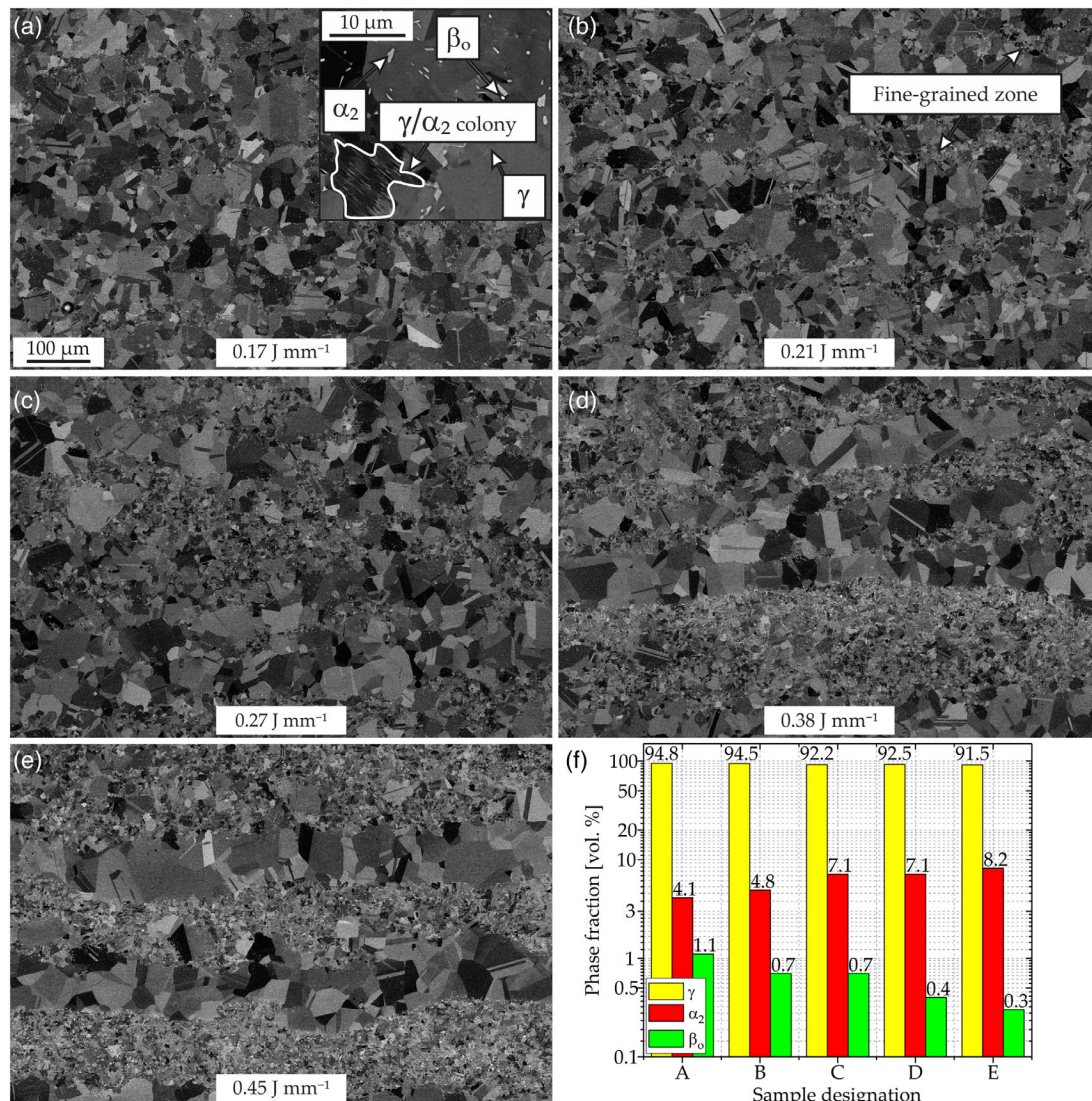


Figure 1. SEM–BSE micrographs of as-EBM samples A–E (images a–e) revealing a change in microstructural morphology from a coarse-grained, homogeneous near- γ microstructure toward a banded near- γ microstructure, where the coarse γ -grains are accompanied by fine-grained zones (marked with arrows) of γ and α_2 and scarce β_0 . As a measure of the energy input into the powder bed, the respective E_L is indicated in the micrographs. The microstructural constituents are marked in the inset in (a), where the globular γ -, α_2 - and β_0 -phase are outlined as well as the silhouette of the remains of a γ/α_2 -lamellar colony. f) Shows the results from quantitative phase analysis by XRD for each of the samples, indicating that the change in overall chemistry and microstructural morphology is accompanied by a shift in the as-EBM phase composition.

increasing energy input realized by an increased beam current and/or a decreased scan speed, the microstructure in sample B (Figure 1b) reveals fine-grained zones, which are marked with arrows. By increasing the E_L further, as seen for sample C in Figure 1c, fine-grained zones seem apparently expanded to wider regions. In sample D, with its microstructure shown in Figure 1d, the fine-grained zones start to emerge in a banded fashion, with alternating layers of coarse-grained γ -bands and fine-grained zones of γ - and α_2 -phase. When it comes to sample E (Figure 1e), the banded, or layered, the microstructure is vigorously noticeable. By changing the process parameters, that is, increasing the energy input, a transition from a comparably coarse-grained near- γ microstructure via an increased amount of fine-grained zones of γ and α_2 (as called duplex like fine

grains,^[27] or fine two-phase region of γ and α_2 ,^[37]) in both, globular and, more rarely, lamellar constitution, becomes clear and, finally, manifests itself fully banded with an E_L of 0.45 J mm^{-1} used for sample E. The coarse γ -grains, that occupy most of the microstructure of low E_L samples (A, B), transform into a sandwiched structure between these fine-grained areas of γ and α_2 by increasing the E_L . The formation of banded microstructures in EBM Ti–48Al–2Cr–2Nb is, therefore, always linked to the respective process parameter-related history. The formation of this layered microstructure can be suppressed, and supported, by choosing respectively appropriate process parameters. It should be noted that the layer-wise manifestation of the microstructure is not constant, and shows varying band thicknesses, which has also been noted before.^[27] The reason is addressed later in this

article. Not only does the microstructure differ as a matter of process parameters but also the porosity, as listed in Table 1, does. While sample A showed a porosity of 0.85%, with increasing energy input the porosity decreased, as sample B revealed a value of 0.24%, followed by sample C with a porosity of 0.11%, sample D with 0.08% and, finally, sample E with 0.04%. Two types of pores appear in electron beam melted TiAl alloys: pores, which are elongated perpendicular to the building direction that reveals a lack of fusion between adjacent melting layers, and spherical pores stemming from Ar entrapment, which was originally entrapped in the powder particles during their production.^[22] Both samples A and B showed a lack of fusion porosity, which typically can be prevented by adjusting the processing parameters accordingly, as also shown with this parameter study. For the other specimens only spherical pores were recorded. It is important to note that the first signs of microstructural inhomogeneity appeared in sample B, which had not been manufactured with an adequate energy input to result in dense specimens without a lack of fusion-induced porosity. Thus, at least slight microstructural inhomogeneity with fine-grained zones, or banded microstructures, as for the samples D and E with high energy input, appears to be an appendage hard to prevent when manufacturing properly dense EBM Ti–48Al–2Cr–2Nb specimens. Hardness measurements according to Vickers, displaying the influence of the processing parameters on the macroscopic mechanical properties, are also shown in Table 1. Sample A behaved the softest, showing 221 HV10. With increasing energy input during manufacturing, the hardness value increased to 225 HV10 for sample B and 229 HV10 for sample C. 234 HV10 was measured for sample D. Sample E, finally, was the hardest, revealing 261 HV10, leading to a difference in HV10 values of 40 for the same alloy manufactured with different processing parameters. This corresponds to an increase in macroscopic hardness of 18% for the same alloy by altering the process parameters of EBM. The reasons for this deviation in macroscopic hardness values are twofold. First of all, microstructures appear increasingly fine-grained with an increase in the energy input in terms of E_L , which leads to an increased strength which is expressed as an increase in macroscopic hardness.^[53,54] The second reason becomes apparent with the results from the quantitative phase analysis via Rietveld refinement on X-ray diffraction (XRD) data, presented in Figure 1f. Not only does the overall chemistry change considerably with regard to the processing-related history but also the phase composition of the samples in their as-EBM state varies. As discussed in Section 1, apart from the very top, most parts of the microstructure of EBM TiAl alloys are explainable by long-term annealing at a respective building temperature. When combining this circumstance with the fact that the respective chemistry for electron beam melted TiAl alloys is a matter of the processing parameters, an explanation for different resulting volume phase fractions for different process parameters is obtained. Samples A and B are similar in phase fractions, with 94.8 and 94.5 vol% γ -phase in addition to 4.1 and 4.8 vol% α_2 -phase besides traces of β_0 in the range of 1.1 and 0.7 vol%. By increasing the E_L the amount of γ -phase decreases to 92.2 vol% for sample C, while the phase fraction of α_2 increases to 7.1 vol%. As the chemistry undergoes a shift to the Al-lean side by increasing the energy input during the process, the phase fractions resulting from an approximated

equilibrium state at the building temperature of the respective process also shift toward the Al-lean side of the Ti–Al–Cr–Nb(–O) phase diagram. The volume phase fractions are similar for sample D with 92.5 vol% γ , 7.1 vol% α_2 , and 0.4 vol% β_0 . The highest energy input in sample E resulted in 91.5 vol% γ , 8.2 vol% α_2 , and 0.3 vol% β_0 . With increasing energy input the amount of γ -phase, therefore, decreased by increasing the α_2 -phase fraction. The γ -phase is softer than α_2 ,^[55] which is another contribution to the differences in established HV10 values for specimens manufacturing with different E_L . Apart from that, the measured phase fraction of the β_0 -phase does decrease as well. Still, differences in the phase fraction of β_0 are marginal and might simply submerge within the error of the Rietveld refinement.^[56] Since the small amount of β_0 -phase does not appear to have an influence on the microstructural formation of EBM Ti–48Al–2Cr–2Nb, the issue was not pursued further within this work.

In Figure 2a, results of the thermomechanical analysis (TMA) measurements as normalized derivative curves of the displacement are drawn over the temperature for each of the specimens investigated. Represented by the peak temperature,^[57] the α -transus temperature ($T_{\alpha T}$) does shift with a change in process parameters. With Al evaporation, and, therefore, the change in overall chemistry, the peak temperature undergoes a change to lower temperatures. The established $T_{\alpha T}$ are listed in Table 1 for each of the specimens, which is 1367 °C for sample A, 1362 °C for sample B, 1356 °C for sample C, 1348 °C for sample D, and 1342 °C for sample E. To visualize the effect on the phase transformation temperature with Al loss, as a consequence of evaporation during the process, a calculated isopleth section via the computer coupling of phase diagrams and thermochemistry (CALPHAD) method for the Ti–Al–Cr–Nb system is displayed in Figure 2b. It should be noted that the calculated section keeps the ratio of Ti:Cr:Nb constant at 48:2:2, which is more representative for the EBM process, as the percentages of Al lost by evaporation during EBM are not solely filled upon with Ti, but in the ratio of 48:2:2 with Ti, Cr, and Nb. It was simplified that neither Ti nor Cr or Nb suffer from the same volatility to evaporation as Al in the Ti–48Al–2Cr–2Nb alloy. This isopleth section is, therefore, more suited to represent the change in overall chemistry during EBM than a quasi-binary section of $(100 - x - 4) \times \text{Ti} - x \times \text{Al} - 2 \times \text{Cr} - 2 \times \text{Nb}$. The phase-field regions are indexed with the respective phases and the nominal composition of the Ti–48Al–2Cr–2Nb alloy at 48 at% Al is marked with a dotted vertical line. The intersection with the $\alpha + \gamma \rightarrow \alpha$ phase-field line marks the $T_{\alpha T}$ at a temperature of 1372 °C. Furthermore, the overall chemistries according to Table 1 and the established $T_{\alpha T}$ for the specimens are marked in the diagram. The $T_{\alpha T}$ are only slightly overestimated by the thermodynamic calculations compared to the experimental results, ranging from 1.5 °C for sample E to 8.0 °C for sample B, and, therefore, can be considered as excellent approximations. Additionally, the T_0 -temperatures were calculated as a function of the Al content for the liquid ($L \rightarrow \beta$), ($L \rightarrow \alpha$), and ($\alpha \rightarrow \gamma$) phase-pairs and added to the diagram as curves. As such, the T_0 temperatures represent the respective temperature, at which the Gibbs free energies of the chosen phases are ident. For a phase transformation to happen the free energy of the transformation product has to be lower than the free energy of the starting phase,^[58]

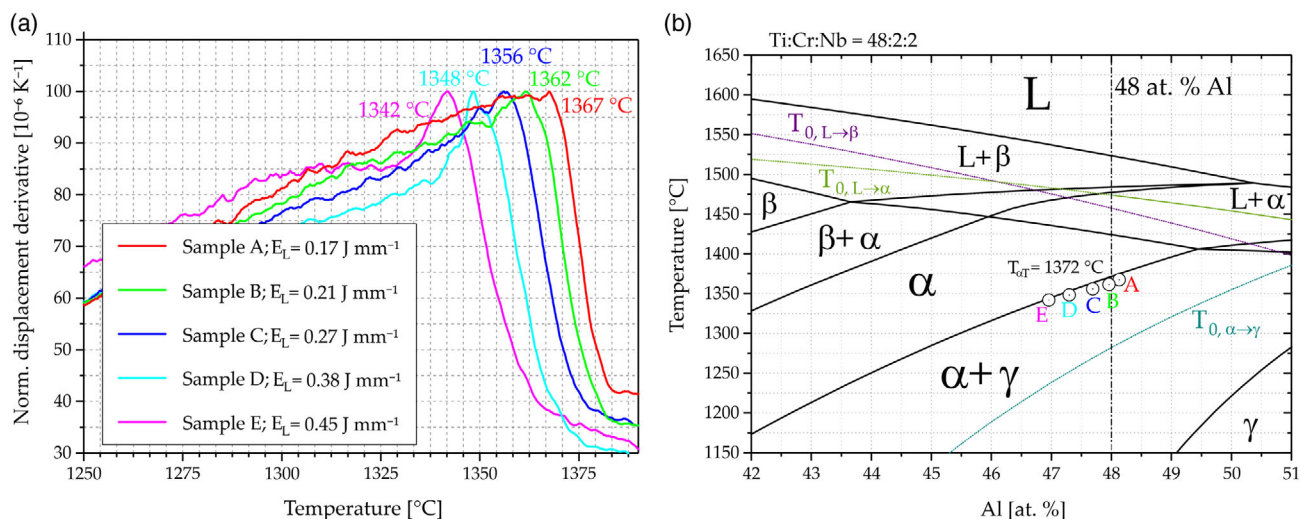


Figure 2. Results from the TMA measurements are shown as normalized displacement derivative curve over the temperature for samples A–E in (a). The established T_{eT} based on the peak temperatures are inserted. Results were translated into the isopleth section in (b) for the Ti–Al–Cr–Nb system and a constant ratio of Ti:Cr:Nb = 48:2:2. The respective phase-field regions are indexed with the stable phases and the Ti–48Al–2Cr–2Nb composition is marked with a dotted vertical line. The calculated T_0 curves for $L \rightarrow \beta$ (purple), $L \rightarrow \alpha$ (olive), and $\alpha \rightarrow \gamma$ (turquoise) are drawn as well.

decreasing the Gibbs free energy of the system overall. In terms of a phase transformation with limited diffusivity, a phase transformation may not happen before reaching that respective temperature. The use of the T_0 -curves is discussed later on.

The choice of EBM process parameters for a Ti–48Al–2Cr–2Nb alloy, therefore, does change the outcome in terms of local and overall chemistry, phase transformation temperatures, microstructural appearance, quantitative phase composition, and, as a direct consequence of the point aforementioned, also the hardness. However, not only the overall chemistry does shift in accordance with the change in processing parameters but also the chemical distribution of the evaporation-volatile Al depends on the respective process parameters.^[34,36] It is, therefore, paramount to investigate the influence of the process parameters not

only on macroscopic characteristics such as overall chemistry, phase fractions, and hardness but also on the microscopic scale based on the chemical distribution. Electron probe microanalysis (EPMA) measurements were utilized to illustrate these characteristics for process parameters used in this study, with the results being shown as SEM–BSE images paired with their respective quantified elemental concentration maps for Al in at% in **Figure 3**. Whereas sample A (**Figure 3a**) and sample B (**Figure 3b**) revealed very homogeneous chemical distributions of Al on the microscopic scale, an E_L of 0.27 J mm^{-1} for sample C (**Figure 3c**) resulted in the appearance of banded characteristics in the elemental distribution map. As the energy input was further increased to 0.38 J mm^{-1} (sample D, **Figure 3d**), a banded appearance of the microstructure, more precisely of Al-lean

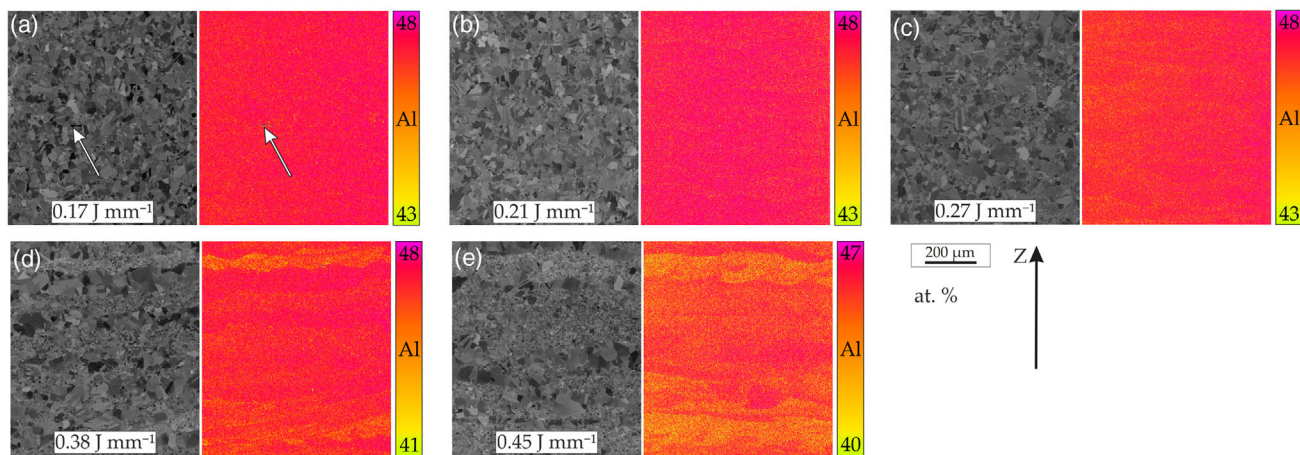


Figure 3. Results from the EPMA investigations show the elemental distribution maps for Al in at% for sample A–E (images a–e) together with the associated microstructure images. Measured Al concentrations change with different process parameters, ranging from 43 to 48 at% for sample A–C, from 41 to 48 at% for sample D, and 40 to 47 at% for sample E. Starting from the low E_L (sample A and B), the Al distribution becomes increasingly heterogeneous when moving toward the high E_L sample (sample E), revealing pronounced banded features with a disparate layer thickness and deviations from a perfect banded structure. The black arrow denotes the building direction Z, whereas the white arrows mark the lack of fusion porosity in (a).

zones, becomes visible. Fine-grained zones, as observed in the general microstructures of samples C, D, and E (see Figure 1) are attributed to these Al-depleted areas. Finally, sample E (as shown in Figure 3e) revealed the highest degree of chemical inhomogeneity on the microscopic scale. With increased rates of evaporation, an intrinsic homogenization does not seem possible due to the low time in the liquid state and large melt bath fluctuation.^[34] Therefore, only samples A and B, where also lack of fusion porosity was observed, show the chemical homogeneity of Al. Regions of large γ -grains represent Al-rich regions in EBM Ti-48Al-2Cr-2Nb, whereas Al-depleted zones are generally richer in α_2 , and, as previously mentioned, fine-grained. The deviations from sharp layer-wise appearances of the chemical distribution of Al, or varying band thicknesses, can be attributed to the stochastic nature of the powder bed (particle size, shape, and distribution in the powder bed), instead of a solid substrate, creating a more complex state of mixing.^[34,40] It should be noted that the measured minimal Al contents change from values of ≈ 43 at% for samples A, B, and C to 41 at% for sample D, with increasing energy input, and, therefore, a change in chemical composition attributed to Al-lean measurement spots in the EPMA elemental distribution maps. Even more, sample E revealed a minimal measured value of ≈ 40 at% besides a decrease of the maximal Al-value to ≈ 47 at%, compared to ≈ 48 at% for all other samples due to the even stronger change in overall chemistry. As such, the specimens take upon a different placement in the phase diagram (see Figure 2), also resulting in different equilibrium phase compositions. As the focus of this study was on the distribution of Al in the microstructure after the EBM process, the respective equilibrium compositions of the phases and the influence of processing parameters on it are the topic of ongoing investigations and are not further discussed. It is noteworthy that the other elements in the alloy, that is, Ti, Cr, and Nb, revealed no process-related preference in their whereabouts, whereby the respective distribution maps are not shown. Lack of fusion porosity can be seen as a black area in the SEM-BSE image, as well as the elemental composition map for sample A (lowest energy input of 0.17 J mm^{-1} , Figure 3a) and is marked with white arrows and the building direction Z, is denoted by the black arrow.

Lack of fusion porosity in electron beam melted Ti-48Al-2Cr-2Nb is most often found below regions of large γ -grain bands and above fine-grained zones that are, as discussed, Al depleted. Such pores are shown in the visible light microscopy image in Figure 4 and marked with blue arrows, whereas spherical porosity due to Ar-entrapment is marked with magenta arrows. As these pores exclusively form between adjacent powder layers during the manufacturing process when the process parameters and conditions are not optimized,^[22] in contrast to the aforementioned spherical porosity, it can, indeed, be concluded that the Al-depletion happens toward the top of the melt pool and, Al-enriched zones (or rather, non-Al-depleted zones), present as large γ -grains, make up the regions toward the bottom of melt baths. This is consistent with an Al evaporation from the top of the melt pool. For this reason, it is very important to compare the different process parameters in terms of maximum temperature reached, area of the generated melt pool, and the total time that the melt pool stays in the liquid phase.



Figure 4. Visible light microscopy image of the occurring porosities in EBM Ti-48Al-2Cr-2Nb. Whereas spherical pores stem from Ar-entrapment (magenta arrows), elongated pores between adjacent powder layers form due to unfavorable process parameters (blue arrows). This lack of fusion porosity exclusively appears below the large γ -grain bands, which, therefore, represents the non-Al-depleted zones toward the bottom of melt baths. The building direction is upwards.

3. Numerical Simulation

From the numerical point of view, it is possible to investigate the thermal history of each sample. From a thermal point of view, the process is mainly featured by the number of remelting events, the achieved maximum temperature, and the dimensions of the melt pool. All together these parameters impact the total holding time above the solidus temperature (T_{Solidus}) and, therefore, the time in which the material is surely in the liquid state, which enables the evaporation of Al and, subsequently, influences the homogeneity of the microstructure. Figure 5 shows the

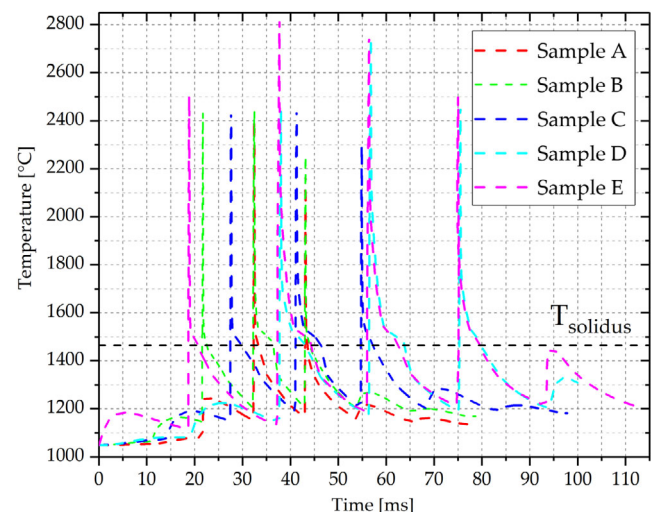


Figure 5. Simulated thermal histories for the specimens A–E, which differ greatly in the amount of remelting events they underwent and the maximum peak temperatures that are reached. The differences are best illustrated by sample A (red) and E (magenta), where sample A was only remelted twice and reached peak temperatures of ≈ 2400 °C and sample E was remelted four times and reached peak temperatures of ≈ 2800 °C. The T_{Solidus} is marked with a dotted black line.

numerical results in terms of thermal histories, which were compared with the T_{Solidus} of the material (dotted black line). Since the same domain was used for all simulations, the thermal history of each sample was collected in the same node of the domain. The simulation of the melting of a layer of sample A has shown the lowest number of remelting events (two) and the lowest peak of temperature (around 2400 °C). The numerical calculations for samples B and C have displayed only a slightly higher maximum temperature (around 2450 °C) with respect to sample A, but the material is subjected to three thermal cycles. For samples D and E, the maximum temperatures are comparable (around 2800 °C), but the sample E showed four remelting events with respect to the three detected for the sample D. From these thermal profiles over time the total holding time in the liquid state was calculated as the cumulative time in which the material is above the T_{Solidus} and is listed in **Table 2** together with the melt pool dimensions in terms of width, length, and area. The straight green line in **Figure 6** shows the calculated times, while the red bars indicate the melt pool area. During the melting of sample A, the formed melted pool area is small (1.61 mm², Table 2) compared to the other samples. With the

Table 2. Results of the numerical simulation listing the calculated holding times in the liquid state as the cumulative time above the T_{Solidus} extracted from the temperature profiles (see Figure 5) in addition to the widths, the lengths, and the areas of the respective melt pools of samples A–E

Sample designation	Holding time in the liquid state [ms]	Melt pool width [mm]	Melt pool length [mm]	Melt pool area [mm ²]
A	1.56	0.44	3.50	1.61
B	6.35	0.65	11.08	3.57
C	10.48	0.64	12.73	5.05
D	17.68	0.65	12.96	5.82
E	20.15	0.67	17.00	8.91

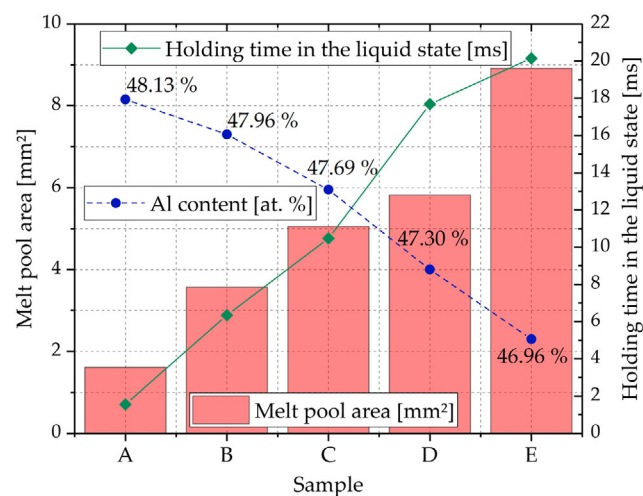


Figure 6. Calculated holding times in the liquid state (green straight line) and the melt pool area (red bars) as well as the overall Al-content (dotted blue line, see Table 1) drawn for the specimens A–E. With a process induced increasing holding time in the liquid state and larger melt pools, the evaporation of Al during the process does increase considerably.

lowest number of remelting events and the lowest maximum temperatures with respect to the thermal histories of the other samples, the holding time in the liquid state for sample A is at least one order of magnitude lower than samples D and E. During the melting of sample B, the formed melt pool area is around twice the size of sample A (3.57 mm² compared to 1.61 mm²) and the holding time above the melting temperature is around four times higher (6.35 ms compared to 1.56 ms). Samples C and D showed similar melt pool lengths, widths, and areas. However, the holding time in the liquid state for sample D is 1.7 times higher than sample C. Sample E showed the largest melt pool (around 8.91 mm²) and a holding time in the liquid state more than 10 times higher than sample A and twice the time of sample C. For easy comparison, the Al content of each sample according to Table 1 is also reported in Figure 6 as a dotted blue line. As can be observed the loss of Al gets increased by increasing the holding time in the liquid state and the melt pool area. Both factors, therefore, can explain the differences in the Al content among the samples and the observed differences in the microstructure. The samples showing higher Al loss (increasing from sample A to E) and, thus, more heterogeneous microstructures, suffered from longer holding times in the liquid state and/or from longer as well as larger melt pools. The holding times in the liquid state do differ as to the peak temperatures of the melt pool and the amount of remelting events is different for the samples. In general, Al loss can be controlled and reduced by processing TiAl alloys in such a way, that the melt pools remain comparably short and small, the peak temperatures stay low and the same positions get remelted fewer times. A compromise is required to reach fully dense specimens and sufficiently homogeneous microstructures with Al contents within the specification. As the samples with higher energy input (e.g., specimens D and E) suffer from a considerably larger amount of Al evaporation banded regions of fine-grained zones of γ and α_2 are formed consecutively.

4. The Formation of Banded Microstructures

The formation of these fine-grained zones, ranging from duplex-like microstructures to lamellar colonies, which are Al-lean and remain preferably in Al-depleted regions due to increased levels of evaporation, can be attributed to the appearance of predominantly α_2 . **Figure 7** shows results from electron backscatter diffraction (EBSD) measurements for all specimens, where the different phase distribution, as a consequence of the combination of long-term annealing at the building temperature while suffering from a possible inhomogeneous distribution of Al, is visible. The α_2 -phase is indexed in red with high angle grain boundaries (HAGB) with a misorientation angle $\theta \geq 10^\circ$ are shown as black lines, while γ -grains (and, very rarely, β_0) were not colored to increase clearness and makeup all the remaining grains. It becomes apparent that α_2 is more homogeneously distributed in low energy input samples, that is, samples A and B. **Figure 7a** depicts the EBSD measurement for sample A, with a comparably homogeneous distribution of α_2 and large γ -grains. With increasing energy input (sample B, **Figure 7b**) α_2 does appear in proximity of fine-grained γ -phase. The issue becomes significantly more notable with increasing energy input, as

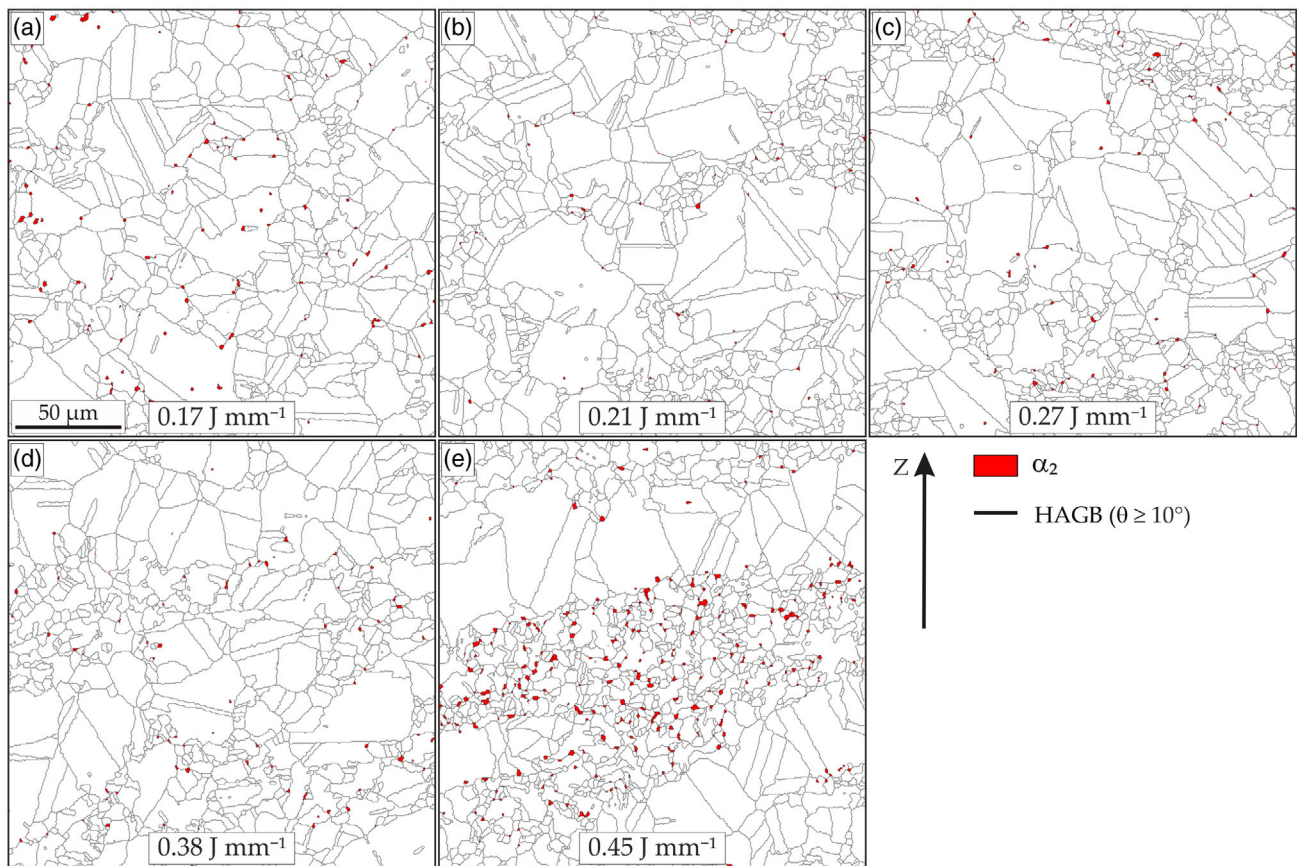


Figure 7. α_2 -phase maps from EBSD measurements on samples A–E (images a–e). Additionally, the HAGB ($\theta \geq 10^\circ$) are drawn to visualize the grain structure. The remaining phases, γ and β_0 , are not colored to increase visibility. It is apparent that sample A (a) with a low E_L of 0.17 J mm^{-1} has a homogeneous α_2 -distribution. With increasing E_L α_2 appears increasingly concentrated, sitting at the grain boundaries of fine γ -grains, indicating abnormal grain growth of γ -TiAl during the EBM process for Ti–48Al–2Cr–2Nb. Fully fledged banded microstructures, as seen for sample E (e) reveal concentrations of α_2 in fine-grained zones sandwiched between γ -grain bands. Samples B–D (images b–d) take on intermediate states and show the progression of the banded microstructure with an increase in E_L .

sample C (Figure 7c) and sample D (Figure 7d) show, that in their bimodal microstructures α_2 has preferable whereabouts in the proximity of fine-grained zones of γ -phase. Once again, specimen E (Figure 7e) revealed the most extreme state in terms of microstructural heterogeneity, with a banded microstructure consisting of large γ -bands and fine-grained zones filled with α_2 -phase. Therefore, with an increase of the inhomogeneous state of Al distribution, not only does the microstructure receive a banded nature but also the whereabouts of α_2 become increasingly localized in Al-depleted regions, apart from the fact that with an increase in heterogeneity also the phase fraction of α_2 does increase, as discussed previously (see Figure 1f). It becomes apparent that grain growth during EBM, leading to γ -grain bands in samples with heterogeneous Al distribution, is inhibited in α_2 -rich areas via Zener pinning,^[59,60] as a part of the long-term intrinsic annealing in the course of EBM. The γ -grains in α_2 -lean areas coarsen up, as grain boundaries are not pinned during the long-term intrinsic annealing, and abnormal grain growth (also called discontinuous grain growth or secondary recrystallization) happens.^[61,62] Grain boundaries are considerably pinned in areas with a higher amount of α_2 , which acts as second-phase particles during EBM, and the overall grain size stays small. As sample A

shows not only a smaller fraction of α_2 but also a more homogeneous distribution than sample E, the just mentioned effect does not occur and the microstructure coarsens up during EBM more homogeneously without the formation of a banded microstructure. This is a direct consequence of the long-term annealing at the elevated building temperature. In contrast, in the case of sample E, there is an inhomogeneous phase distribution as a consequence of an inhomogeneous Al chemical distribution. We discussed this issue comprehensively in a previous publication.^[43] The banded nature of some microstructures of electron beam melted Ti–48Al–2Cr–2Nb is, therefore, the consequence of a process related to inhomogeneous Al distribution coupled with the high amount of γ -phase in thermodynamic equilibrium at the building temperature for this alloy, leading to abnormal grain growth in α_2 -lean areas, where the influence of second-phase particles on grain boundary movement is diminished.

It has been shown that banded TiAl microstructures exhibit anisotropic mechanical properties showing low RT ductility.^[25,27] Thus, local mechanical properties indicating anisotropic properties do need investigation. The local mechanical properties of EBM Ti–48Al–2Cr–2Nb are displayed in Figure 8 depicting the microscopic hardness mappings according to HV0.05

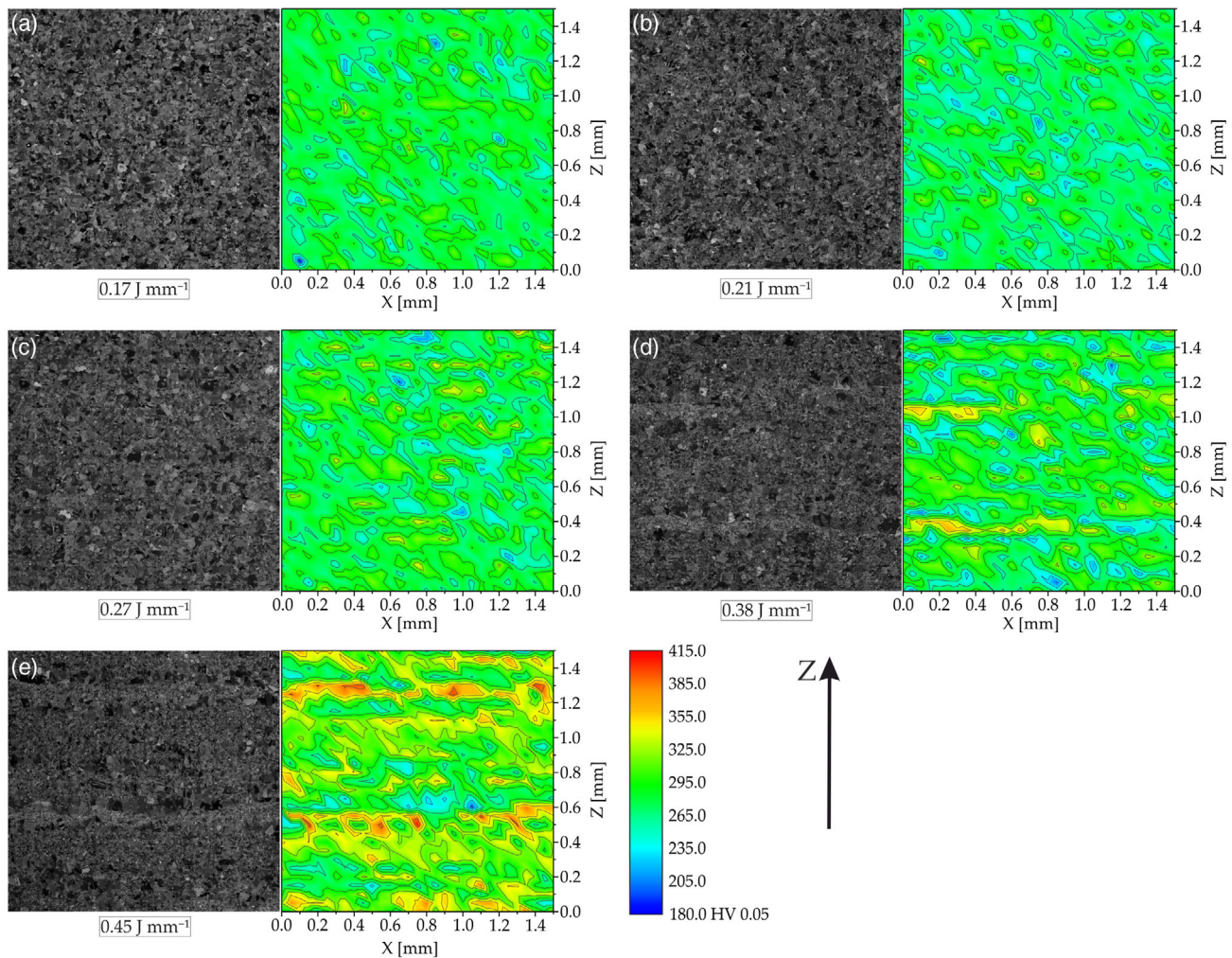


Figure 8. HV0.05 hardness maps with the respective SEM–BSE image of the indented area. Samples A and B (images a,b) revealed no banded features of the measured hardness values, which are comparably low, as mostly large γ -grains are indented. With increasing line energy (samples C and D, images c, d) regions with increased hardness values are distinguishable, with slight hardness bands for sample D. These regions can be attributed to the fine-grained zones of γ and α_2 . Increasing the energy input to 0.45 J mm^{-1} (sample E, shown in e) leads to the microstructure with the highest HV0.05 values, ranging beyond 400 HV0.05, and showing high variations in hardness as well as a banded nature.

generated on samples A–E accompanying the microstructure obtained with SEM–BSE. The microscopic mechanical properties directly reflect the microstructure observed and described previously. As sample A (Figure 8a) and sample B (Figure 8b) have microstructures consisting mostly of large γ -grains accompanied by smaller amounts of α_2 hardness is, thus, mostly low with values $\approx 295 \text{ HV0.05}$, as γ is, generally, the softest phase in the Ti–48Al–2Cr–2Nb alloy.^[55] HV0.05 values ranged from 180 to 339 for sample A, and from 206 to 348 for sample B. Furthermore, the microscopic hardness is comparably homogeneous, as were the microstructures. An increased E_L sample C, which previously revealed pronounced fine-grained zones with slight accumulations of α_2 , (SEM–BSE image in Figure 8c), shows sections of the microstructure, where higher HV0.05 values were measured, reaching from 200 up to 381 HV0.05. This circumstance can be attributed to the increased hardness due to finer grains,^[54] and, additionally, the increased amount of α_2 -phase in these regions. Sample D (Figure 8d) illustrates that the occurrence of banded

microstructures, as is the appearance of a banded allocation of α_2 in fine-grained zones, leads to bands of increased microscopic hardness up to 372 HV0.05, whereas indenting large-grained γ -bands resulted in lower hardness values down to 205 HV0.05. Paying attention to sample E (Figure 8e), the microscopic hardness appears in a widely banded fashion with the highest values up to 409 HV0.05, revealing a considerably more inhomogeneous state of anisotropic mechanical properties. It is interesting to note that the minimum values were always in the range of $\approx 200 \text{ HV0.05}$ for all samples (apart from sample A, probably partly due to the significantly increased porosity), indicating positions with either large γ -grains, or similar, γ -grain bands. Part of the γ -grains in low E_L samples are replaced in high E_L samples with α_2 -rich fine-grained bands, whether it may be in fine globular $\gamma/\alpha_2/\beta_0$ -grains or as γ/α_2 -colonies, which are responsible for high hardness, surpassing even 400 HV0.05. Grains stay fine during EBM in these Al-lean regions due to the Zener pinning force of second-phase α_2 -particles on the grain

boundary of the γ -phase, while, in general, there is a constant tendency to generate a microstructure of coarse γ -TiAl for the near- γ microstructures that are the thermodynamic equilibrium condition at the building temperature.

In summary, banded microstructures of large γ -grain zones and fine-grained zones containing γ and α_2 are the consequence of the long-term intrinsic annealing at the building temperature, coupled with an inhomogeneous Al distribution. Process-related evaporation of Al leads to Al-depletion toward the top of the melt pool and non-depleted zones toward the melt pool bottom. Grain growth during the EBM process coarsens γ in the non-Al-depleted regions, while α_2 predominantly remains in Al-lean zones, leading to Zener-pinning of γ -grain boundaries. With a change in energy input, exemplarily expressed as E_L , the rate of evaporation, as well as the state of heterogeneity of the microstructure, can be influenced, affecting overall chemical composition, phase fractions, and Al-distribution. Banded microstructures are coarse γ -grain microstructures where the through-out grain growth during the process was suppressed by an increased amount of second-phase particles in a banded fashion, as the Al-lean α_2 -phase preferably dissolves in non-Al-depleted zones. Banded microstructures in Ti-48Al-2Cr-2Nb can be inhibited by reducing the maximum peak temperatures, melt pool sizes, and holding times above the T_{Solidus} during EBM by decreasing the energy input through lowering Al-evaporation and generating a homogeneous Al distribution, with acceptable levels for samples A–C.

5. Solidification and Intrinsic Annealing during EBM

The last layers of consolidated material in EBM TiAl alloys have already received some attention. Microstructures on the very top of the as-EBM specimens are described as nearly lamellar,^[24,38] partially with equiaxed γ and blocky β_0 , or fully lamellar.^[27,30,48,51] Epitaxially grown, elongated grains, shrinking with lower energy input, were described as well, and resembled massive γ -grains.^[36] Explanations for the microstructural formation subsequently involve the change in annealing temperatures as subsequent layers are built upon,^[27] or the heat treatment during the process.^[51] The bottom-up microstructural evolution of EBM Ti-48Al-2Cr-2Nb can, therefore, be considered to be the result of the decreasing cyclic annealing temperature as subsequent layers are added above. Focused studies on the solidification behavior of EBM Ti-48Al-2Cr-2Nb, especially with regard to the process parameters, as well as the intrinsic annealing with respect to the aforementioned parameters, are still absent. **Figure 9** displays microstructures toward the top (marked with T) of the built components (marked with red arrows) for samples B and E, taken representatively for a specimen built with low E_L (0.21 J mm^{-1}) and one with a high E_L (0.45 J mm^{-1}), for both of which the job was concluded directly after the last melting, thus, avoiding the last post-heating, as described in Section 8. It becomes apparent from the high magnification micrographs for both E_L in Figure 9a,b that the microstructures on the top do, in fact, constitute lamellar colonies of γ and α_2 , but are different due to the change in processing parameters. Whereas sample B shows rather small lamellar colonies accompanied

by globular α_2 and some γ -grains, sample E reveals large γ/α_2 -colonies, which are elongated in building direction. Although lamellar orientations appear perpendicular to the building direction Z, the occurrence is stronger pronounced in sample E. As sample B does contain considerably higher amounts of Al than sample E (≈ 1 at%, compare Table 1), the driving forces for the formation of globular γ by are expected to be significantly higher during the slow cooling to RT after the completion of the process (see temperature development after process completion in Section 8 and Figure 15), which leads to partial decomposition of the colonies. Additionally, certain amounts of γ might already form during cooling while still in the melting step of the EBM process. Schwerdtfeger and Körner,^[36] reported the possibility for massive transformation due to the high cooling rates, even though they used a lower build temperature of 910°C . As illustrated in Figure 2b as a turquoise line, the $T_{0,\alpha\rightarrow\gamma}$ curve is a strong function of the Al content and does decrease considerably with decreasing Al content. The respective calculated $T_{0,\alpha\rightarrow\gamma}$ are listed in **Table 3** for the samples A–E. As massive transformations only involve thermally activated jumps across the α/γ -interface, they cannot happen as long as the condition for a massive transformation, lower free energy of the γ -phase, is not fulfilled. Furthermore, as the massive transformation involves no change in chemical composition, it, therefore, cannot happen above the respective $T_{0,\alpha\rightarrow\gamma}$. As $T_{0,\alpha\rightarrow\gamma}$ continuously drops from sample A (1288°C) to sample E (1236°C), the formation of massive γ becomes more likely for low energy input samples with higher $T_{0,\alpha\rightarrow\gamma}$. In summary, for lower energy input samples the process parameters do favor the formation of globular γ from the decomposing lamellae colonies, be it via higher driving forces due to higher Al content, a more probable massive transformation, or generally lower intrinsic annealing temperatures. The orientation of γ/α_2 -lamellae is related with the parental α -grain via the Blackburn orientation relationship (BOR) $(0001)_{\alpha_2} \parallel \{111\}_{\gamma}$, $\langle 1120 \rangle_{\alpha_2} \parallel \langle 110 \rangle_{\gamma}$.^[63] It is important to note that the $[0001]$ direction is the preferred growth direction of the α -phase,^[64] which leads to lamellar microstructures perpendicular to the growth direction of the α -grain. It has been addressed before that, in general, as subsequent layers are built upon a certain, consolidated material point, the intrinsic heat treatment transforms top-layer lamellar microstructures with dropping annealing temperatures to nearly lamellar, duplex, and lastly, near- γ microstructures.^[27] However, process parameters and local Al-depletion due to evaporation influence that procedure greatly. The effect is first illustrated in Figure 9c, where the low magnification microstructure at the top for sample B is shown. No heterogeneities are visible. Then again, Figure 9d, showing the low magnification microstructure on the top of sample E, already shows banded features in the microstructures just $\approx 500 \mu\text{m}$ from the top, as the microstructure is already adjusted to the local chemistries, with wavy, bright areas, which are Al-depleted. Therefore, a change in process parameters toward higher E_L already leads to a microstructural response around $500 \mu\text{m}$ from the top. Apart from these findings, increasing the E_L up to 0.45 J mm^{-1} leads to a highly uneven and wavy surface of the specimen (compare Figure 9c,d). This is the direct consequence of considerably higher forces determining the melt pool leading to severe melt pool motion,^[65] apart from significant Al evaporation. Microstructures $\approx 6 \text{ mm}$ from the top for

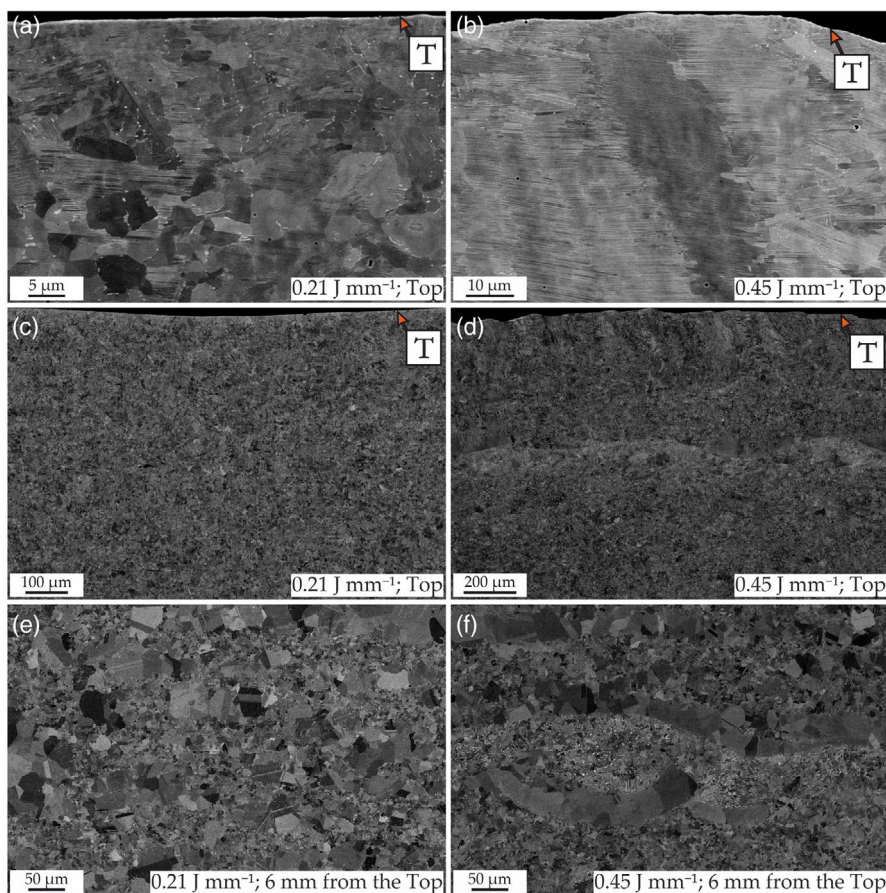


Figure 9. SEM–BSE images of the microstructural evolution from the top (marked with T) of the as-EBM samples B (a) and E (b) in high magnification and in low magnification (images c,d). All microstructures appear fully to nearly lamellar toward the very top, but undergo an annealing treatment approaching the building temperature, illustrated by the SEM–BSE images 6 mm from the top, as shown in images (e,f), where it becomes apparent that early visible heterogeneities translate in different microstructures as a response to the intrinsic annealing already few mm down below.

Table 3. Calculated $T_{0,\alpha\rightarrow\gamma}$ temperatures by thermodynamic equilibrium simulations, which represent the earliest possible temperatures for the massive $\alpha\rightarrow\gamma$ transformation on cooling and the numerical simulation results for samples A–E with the calculated solidification rates and the respective cooling rates from the liquid phase.

Sample	$T_{0,\alpha\rightarrow\gamma,\text{ym}}$ [°C]	Solidification rate [mm s ^{−1}]	Cooling rate [K s ^{−1}]
A	1288	2832	8.99×10^4
B	1281	2849	2.16×10^4
C	1269	2080	1.89×10^4
D	1252	1435	1.57×10^4
E	1236	406	1.96×10^4

samples B and E are shown in Figure 9e,f. As aforementioned, intrinsic annealing in the course of EBM transitions the microstructures from fully lamellar and nearly lamellar toward a near- γ microstructure. Interestingly, the microstructural arrangement is different for samples B and E. The micrograph for sample B depicts a near- γ microstructure, consisting of mostly large γ -grains accompanied by zones of a smaller duplex-like regions,

which transforms fully into a near- γ microstructure (see Figure 1b) with progressing intrinsic annealing. This intermediate state already appears homogeneous. The microstructure of sample E, in contrast, as shown in Figure 9f, adjusts differently to the intrinsic annealing from layers consolidated above. The bottom of previous melt tracks revealed the formation of γ -grain bands, whereas the middle-top regions of the melt tracks are rich in α_2 , present in globular fashion, and colonies with coarsened lamellae width. The microstructure, in general, appears highly heterogeneous. Subsequently, fully banded microstructures are generated on subsequent intrinsic annealing, as can be seen in Figure 1e.

The solidification behavior and successive microstructural features, such as lamellar orientations, are of high importance for the mechanical properties of TiAl alloys,^[64] and understanding solidification behavior remains crucial for the application of TiAl alloys. **Figure 10** displays the inverse pole figure (IPF) maps with respect to the Z direction (building direction) (IPF-Z) for samples A–E at the very top (Figure 10a–e). The lamellar colonies on the top of samples A–E show different morphologies in terms of shape. These colonies on the top have their data points mostly indexed as γ -phase due to the high step size for the fine

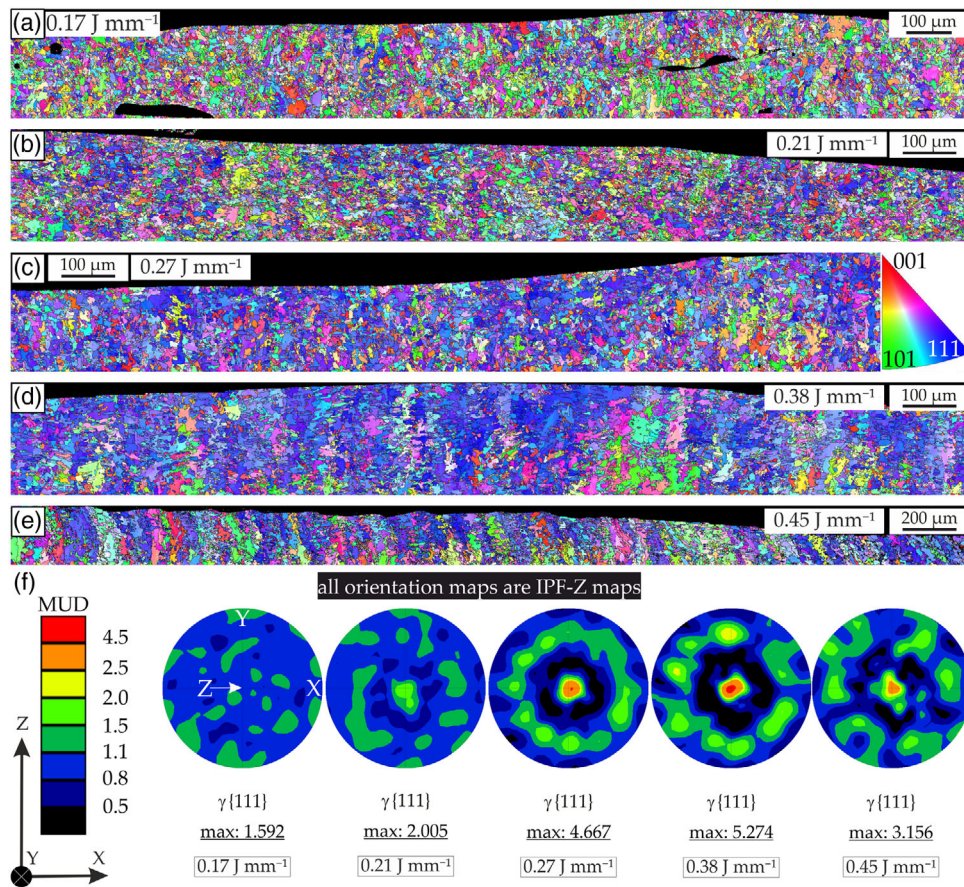


Figure 10. IPF-Z maps of the last consolidated layers for sample A–E (images a–e). With an increase in E_L the grain structure does visible change from equiaxial grain formations (sample A and B) to elongated grains (sample C) and, finally, columnar microstructures for samples D and E. The respective $\{111\}_\gamma$ pole figures are shown in (f). Whereas the $\{111\}_\gamma$ pole figures reveal no pronounced orientations for sample A (0.17 J mm^{-1}), an increasing alignment of $\{111\}_\gamma$ with the building direction Z can be seen for the other samples. The maximal MUD value of 5.274 was measured for sample D, which was manufactured with 0.38 J mm^{-1} .

remaining α_2 -lamellae (which gets exaggerated by the 70° sample tilt) and the subsequent cleanup procedure. Furthermore, as γ is measured as cubic phase (see Section 8), only two of the six variants derived from the BOR are indexable. The shape of the lamellar grain morphology on top is, still, of very high interest and can be derived from the EBSD measurements as well as information about the orientation of the γ -phase. Interestingly, the grain morphology of the lamellar colonies on the top is a matter of the process parameters. Low energy samples (A, B, and Figure 10a,b) revealed globular and equiaxial grain shapes at the top, and sample A, additionally, revealed spherical porosity as well as lack of fusion porosity (visible as unindexed/black areas). With increasing E_L sample C (Figure 10c) revealed some grains with elongated shapes in the building direction. A further increase in energy input resulted in a pronounced columnar grain structure in the building direction for sample D (Figure 10d). Lastly, sample E (Figure 10e), manufactured with the highest energy input, revealed large columnar grains throughout the top layer, similar to the ones shown in Figure 9b. By increasing the E_L , and, in general, the energy input into the sample, the grain structure does modify from equiaxial

grains toward columnar and elongated grains. The energy input during EBM does alter the grain structure of the lamellar colonies, therefore, significantly. Information about the solidification behavior can be obtained by investigating the $\{111\}_\gamma$ pole figures as multitudes of uniform distribution (MUD), as displayed in Figure 10f. Sample A, manufactured with 0.17 J mm^{-1} , revealed no preferred orientations for the $\{111\}_\gamma$ planes and only a maximal MUD value of 1.592. By increasing the E_L to 0.21 J mm^{-1} the maximal MUD value increased to 2.005, also indicating an alignment of $\{111\}_\gamma$ with the building direction Z. By increasing E_L even further, 0.27 and 0.38 J mm^{-1} for sample C and D, maximal MUD increased to 4.667 and 5.274, respectively. Sample E revealed a similar $\{111\}_\gamma$ pole figure, but the maximal MUD decreased to 3.156.

Interestingly, as calculated in Figure 2b, the solidification phase transformation pathway for Ti–48Al–2Cr–2Nb in thermodynamic equilibrium is $L \rightarrow L + \beta \rightarrow L + \beta + \alpha \rightarrow L + \alpha \rightarrow \alpha$, and, therefore, involves a peritectic reaction. As discussed earlier, the building direction Z is, in general, the direction of the highest thermal gradient for the EBM process and can, therefore, be considered the growth direction of solidifying crystals. A primary

solidification via the α -phase favoring the $[0001]_{\alpha}$ direction is indicated if the lamellar orientations are perpendicular to the growth direction, which is, indeed, the case, as seen in Figure 9. When investigating the $\{111\}_{\gamma}$ pole figures it becomes apparent that with an increase in E_L the (111) pole of the γ -phase does align with the building direction of the process, which is parallel to the $(0001)_{\alpha}$, taking the BOR aforementioned into account.

Indeed, it has been shown previously that the α -phase becomes the primary phase during directional solidification if growth rates of 72 mm h^{-1} (0.02 mm s^{-1}) and thermal gradients of 4 K mm^{-1} are surpassed.^[66] As temperature gradients for EBM were reported to be in the range of 10^8 – 10^9 K m^{-1} and solidification rates range from 10^4 to 10^5 m s^{-1} ,^[19] those thresholds are easily exceeded. Nevertheless, in this work, the numerical simulation was utilized to calculate the solidification rates for specimens A–E and are shown in Table 3. In the same way, as the process parameters influence the Al evaporation and, furthermore, the microstructural homogeneity, the solidification rates do also differ. Whereas samples A and B show values of 2832 and 2849 mm s^{-1} , respectively, the solidification rates do decrease for samples C (2080 mm s^{-1}) and D (1435 mm s^{-1}). Specimen E, finally, only obtained solidification rates of 406 mm s^{-1} . However, all these calculated values for the solidification rates exceed the value of 0.02 mm s^{-1} from directional solidification and growth experiments mentioned previously, where the α -phase became the primary solidification product. Explanations can be found in Figure 2b. During rapid solidification, diffusion might be highly limited and equilibrium phase compositions are not achievable. For the nominal Ti–48Al–2Cr–2Nb composition the $T_{0,L \rightarrow \alpha}$ (olive line) is higher than the $T_{0,L \rightarrow \beta}$ (purple line). If certain diffusion limits are reached, α becomes the first phase to become thermodynamically more stable than the liquid phase, neglecting the formation of the primary β -phase and the peritectic reaction during solidification altogether. Indeed, it has been shown before that the solidification behavior for a Ti–48Al alloy during rapid solidification conditions does skip the formation of primary β -phase,^[67] for cooling rates of $1.25 \times 10^3 \text{ K s}^{-1}$ and it has, furthermore, been reported that the cooling rates from the liquid phase for the EBM process are between 10^3 and 10^5 K s^{-1} .^[68] The respective cooling rates for this study were also calculated by numerical simulation and can be found in Table 3. They range from $1.57 \times 10^4 \text{ K s}^{-1}$ for sample D up to $8.99 \times 10^4 \text{ K s}^{-1}$ for sample A, which surpasses the threshold cooling rate mentioned earlier by at least one order of magnitude. Taking all these points into consideration, the rapid solidification and transformation pathway during EBM for Ti–48Al–2Cr–2Nb can, therefore, be summarized as follows: $L \rightarrow L + \alpha \rightarrow \alpha \rightarrow \alpha + \gamma \rightarrow \alpha_2 + \gamma (+\beta_o)$. The reason why no pronounced $(0001)_{\alpha}$ textures are found for EBM Ti–48Al–2Cr–2Nb microstructures far away from the top might be explainable on the one hand by the high amount ($>90\%$) of recrystallized γ -phase found in the microstructures and the immediate cyclic annealing after consolidation, visible via the occurrence of annealing twins (see Figure 1), and, in contrast by the fact that the non-equilibrium heating process deviates even further from equilibrium for Ti–48Al–2Cr–2Nb. It has been shown that for very high heating rates the liquefaction pathway happens via $\alpha_2 + \gamma \rightarrow \alpha_2 + \gamma + L \rightarrow \gamma + L \rightarrow L$,^[69] which might further

impede the formation of macroscopic textures. By investigating the final layer on the very top, it became, anyway, apparent, that the growth of primary α -crystals is a matter of the respective solidification conditions, as they might either appear globular or elongated in building direction Z. Still, macroscopic Al distribution remains the significant factor for EBM Ti–48Al–2Cr–2Nb defining the response to heat treatments, which is explored in the next section.

6. Process Related Heat Treatment Response and Remedial Actions

The mechanical properties of TiAl alloys are very sensitive to the microstructure.^[7] It remains mandatory to hot isostatic press and heat-treat critical TiAl components intended for aeronautical application as an act of security precaution whether they are manufactured by casting,^[20] forging, or AM, as processing-related porosity has to be closed and the microstructure has to be carefully adjusted to the needs of the application. Duplex microstructures show favorable tensile ductility,^[70] and were, therefore, chosen in this work to investigate the influence of process parameters on the microstructural evolution during subsequent heat treatment. Duplex microstructures are obtained by performing annealing treatments in the $\alpha + \gamma$ phase-field region, below $T_{\alpha T}$ and above the eutectoid temperature.^[8] The performed heat treatment consisted of annealing at 1320°C for 2 h, followed by cooling to room temperature with $\approx 125 \text{ K min}^{-1}$, as has been performed previously on an EBM Ti–48Al–2Cr–2Nb alloy.^[22] The same temperature was chosen deliberately for all samples, despite the different overall chemistries. The SEM–BSE micrographs are displayed in Figure 11. First of all, sample A–D (Figure 11a–d) all show duplex microstructures with globular γ -phase, lamellar colonies of γ and α_2 , some α_2 -laths in γ -grains with a gradual increase in the amount of α_2 -phase in the microstructure from sample A to sample D. As the overall chemistry shifts away from the Al-rich side of the phase diagram with an increase in E_L from 0.17 to 0.38 J mm^{-1} (see Figure 2b) the microstructure starts to gradually move from a duplex microstructure toward a nearly lamellar microstructure. At the respective heat treatment temperature, the amount of α -phase is increased in thermodynamic equilibrium for a decrease of the Al-content with an increase in E_L , leading to a different microstructure than the desired one. This means that the process parameters have to be taken into account when setting up heat treatments for the application of EBM Ti–48Al–2Cr–2Nb, and, in general, electron beam melted titanium aluminides. Monitoring the overall chemical composition and $T_{\alpha T}$ is necessary to obtain requested microstructures. Furthermore, not only does sample E (Figure 11e) contain an even higher amount of α_2 in the microstructure after the heat treatment but also large lamellar colonies of γ/α_2 , which occur in a banded fashion. It appears that the inhomogeneous microstructure of the as-EBM state for sample E leads to a distinctly heterogeneous response to the performed heat treatment, with large colony bands occurring perpendicular to the building direction. Leaning on previous studies,^[27] it would be expectable that these microstructures show anisotropic mechanical properties with a lower ductility not desirable for application. So heat-treating EBM Ti–48Al–2Cr–2Nb does not

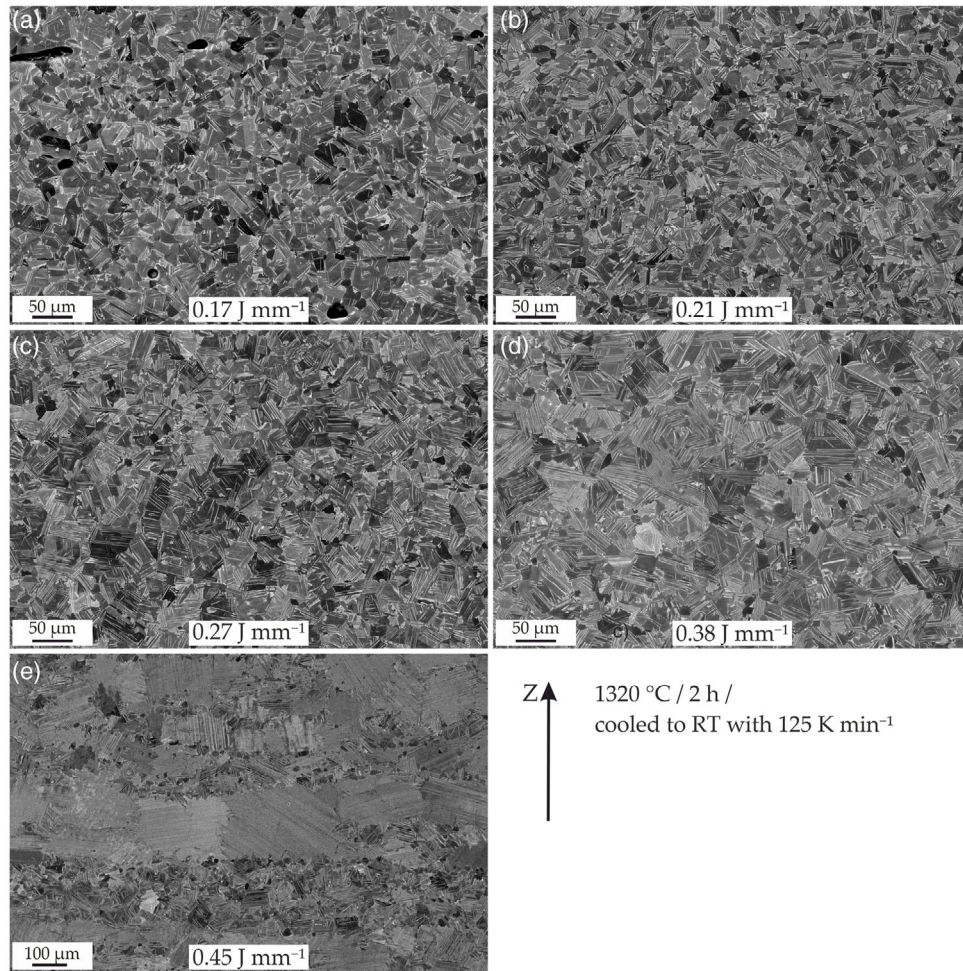


Figure 11. SEM–BSE images of samples A–E (a–e) after a heat treatment at 1320 °C for 2 h, followed by cooling with 125 K min^{−1}. Samples A–D (images a–d) reveal a duplex microstructure of γ and α_2 , arranged in either globular γ (with or without α_2), and γ/α_2 -colonies. With an increase in E_L (and, therefore, an increase in Al loss) the amount of α_2 in the final microstructure gradually increased from sample A to D. Sample E (e), in contrast, revealed a higher amount of large γ/α_2 -colonies, which show a banded morphology. The arrow denotes the building direction Z.

only possess the danger of an Al-evaporation induced shift in the $T_{\alpha T}$ leading to different microstructures than one would expect but also to a banded microstructure subsequently to the heat treatment as a consequence of high levels of inhomogeneity in the as-EBM state.

To investigate this microstructural occurrence an additional, specially designed heat treatment was performed. Sample A, with a low energy input of 0.17 J mm^{−1}, and sample E, with the highest E_L of 0.45 J mm^{−1} were both subject to annealing at 1290 °C for 4 h followed by water quenching (WQ), which was performed to preserve and freeze the microstructural state at the elevated temperature. The associated EBSD phase maps of both samples are shown in **Figure 12**, with the γ -phase indexed in yellow and α_2 indexed in red. In addition, HAGBs are drawn in black. Whereas sample A (Figure 12a) revealed a homogeneous response to the heat treatment in terms of α_2 -distribution along the grain boundaries of the remaining γ -grains, sample E (Figure 12b), as a consequence of its inhomogeneous distribution of Al, shows the formation of an α_2 -band during the heat

treatment. At 1290 °C α -grains grew into each other and, with no γ -grains to pin the grain boundaries, large α -grains simply grew at the expense of small α -grains and formed an elongated band, which, during intermediate cooling, would form a band of lamellar γ/α_2 -colonies in accordance with the BOR.^[63] As these specimens were WQ, the formation of lamellar colonies during cooling was suppressed. The inhomogeneous accumulation of α_2 and, in a broader sense, the inhomogeneous Al distribution due to evaporation effects when providing high energy inputs during manufacturing are directly responsible for the formation of banded microstructures with elongated bands of lamellar colonies while heat treating electron beam melted Ti–48Al–2Cr–2Nb.

To alleviate the influence of inhomogeneous microstructures on the mechanical properties, that is, ductility, the homogenization of the microstructure of TiAl alloys via heat treatments by taking advantage of solid-state transformations is possible.^[71] As the Ti–48Al–2Cr–2Nb alloy possesses a single-phase field region above the $T_{\alpha T}$ (as calculated as 1372 °C for the nominal composition via the CALPHAD method, see Figure 2b), the chemical

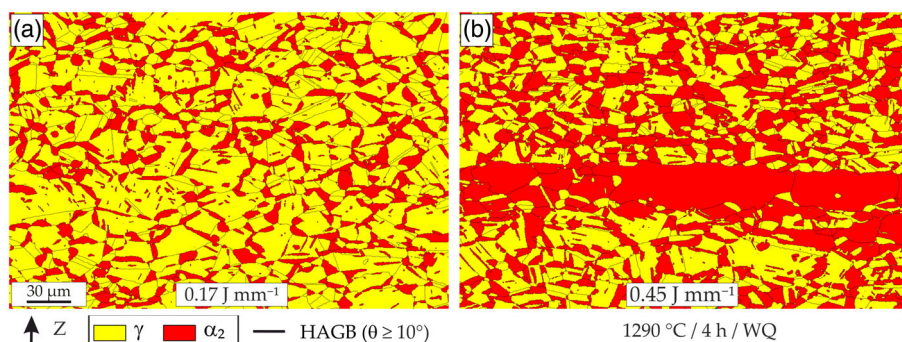


Figure 12. EBSD phase maps of sample A (a) and sample E (b) after annealing at 1290 °C for 4 h, followed by WQ. γ -TiAl is indexed in yellow, whereas α_2 -Ti₃Al is colored in red. HAGBs ($\theta \geq 10^\circ$) are drawn in black to give information on the grain structure. Not only does the process-related history change the amount of α -phase at the annealing temperature but also the whereabouts of the α -phase do change. Sample E revealed a heterogeneous distribution of α -grains growing together and coarsened considerably, leading to an elongated band, which would result in banded γ/α_2 -colonies on subsequent cooling with intermediate cooling rates instead of WQ.

homogenization of Al across the specimen or component is a possibility. For that reason, the heat treatment has to be performed above the $T_{\alpha\gamma}$, otherwise an extended heat treatment would lead to coarsening of the present phases, but no homogenization of Al would take place, as there is no driving force for the homogenization of the whereabouts of phases at their respective equilibrium compositions. Therefore, homogenization has to be performed in the α -single-phase field region. Seifi et al.,^[37] came to a similar conclusion when investigating the microstructural evolution of EBM Ti–48Al–2Cr–2Nb after HIP in the two-phase field region. Another heat treatment was designed to establish whether it truly was a matter of an inhomogeneous distribution of Al and, if yes, for which duration such a homogenization treatment should be performed. **Figure 13** shows the results of the heat treatment performed on sample E, as the microstructure showed the highest degree of inhomogeneity (see previous sections). The heat treatment set-up is depicted in Figure 13a. The starting point for the homogenization is the heat treatment discussed with and shown in Figure 11, but instead of cooling with 125 K min^{−1} the specimens were subject to air cooling (AC). After this heat treatment at 1320 °C for 2 h followed by AC the specimens were subjected to an annealing treatment at 1360 °C in the α -single-phase field region for three different times, that is, 5 min, 30 min, and 1 h. Subsequently, the specimens were quickly cooled to an aging temperature of 1300 °C and held for 2 h, followed by cooling to RT with 125 K min^{−1}. Annealing in the α -single-phase field region for different prolonged times resulted in different amount of times for homogenization of Al, followed by the aging at 1300 °C (in the $\alpha + \gamma$ two-phase field region), which induced a driving force for the formation of γ -grains. Apart from large γ/α_2 -colonies, the microstructure of sample E after 5 min at 1360 °C still revealed the formation of γ -grains that precipitated in a strongly pronounced banded fashion, as seen in the SEM–BSE image in Figure 13b. Increasing the annealing time to 30 min banded γ -grain precipitations still occurred during the aging step, although the amount of γ -grains precipitating within the colonies decreased considerably. The corresponding SEM–BSE micrograph is shown in Figure 13c. When increasing the annealing

time further to 1 h the precipitation of γ did not take place in a banded fashion but instead γ -grains precipitated along the γ/α_2 -colony boundaries without any preference for layer-wise precipitation (Figure 13d). It is concluded that 1 h of annealing in the α -single-phase field region is sufficient to obtain a technically homogeneous state of Al and that, in fact, the inhomogeneous distribution of Al is the origin of heterogeneous microstructures after the intrinsic annealing of EBM and subsequent heat treatments.

So, the pathway to homogenize the microstructure of the electron beam melted Ti–48Al–2Cr–2Nb alloy is illustrated in **Figure 14a**. Annealing for 1 h followed by oil quenching (OQ) lead to the formation of feathery γ (γ_F),^[72,73] a metastable microstructure which consists of most parts of small misoriented domains of several parallel γ -lamellae. Traces of α_2 might also be present. The microstructure after the metastable phase transformation is shown in Figure 14b. As metastable microstructure, recrystallization happens on subsequent annealing, as defect density and the large interface area act as driving forces. This homogenized state was, subsequently, subjected to an annealing treatment recrystallizing the microstructure at 1100 °C for 24 h to form a near- γ microstructure (SEM–BSE micrograph in Figure 14c), which was AC. Exemplarily, a homogeneous duplex microstructure was generated by an additional annealing step at 1320 °C (Figure 14d) without any banded features. The heat treatment procedure, therefore, was able to homogenize the heterogeneous as-EBM state of sample E and enabled the formation of a duplex microstructure missing banded microstructural arrangements. It should be noted that the presented heat treatment route has two limits: first, OQ to RT offers an increased risk of crack formation in TiAl alloys, as OQ involves rapid cooling below the brittle-to-ductile-transition temperature. Additionally, the formation of γ_F during OQ often does not embrace the whole microstructure, as driving forces decline with the γ_F formation, which limits the potential for the generation of fine-grained microstructures during the annealing/recrystallization step.^[73] However, the developed heat treatment route could be used with alloys with a high tendency to perform the massive $\alpha \rightarrow \gamma$ transformation, such as high Nb bearing TiAl alloys, where AC already

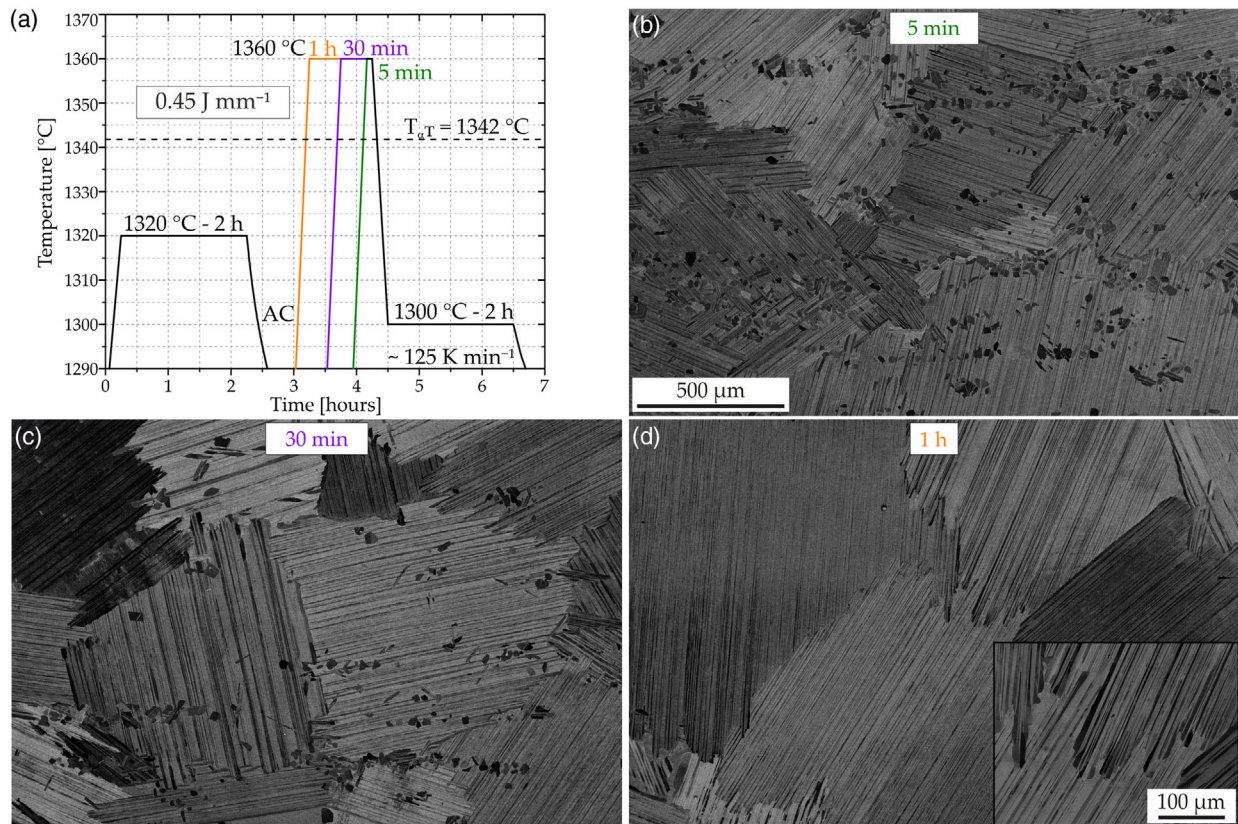


Figure 13. Designed heat treatment route to establish the time required for a homogenization treatment in the α -single-phase region for sample E with the highest E_L of 0.45 J mm^{-1} . The heat treatment route is shown in (a), where, subsequently to the heat treatment step similar to the one shown in Figure 11, the specimen was annealed for 5 min (dark green), 30 min (purple), and 1 h (orange) in the α -single-phase field region at 1360°C , followed by an annealing step at 1300°C for 2 h. Finally, the specimen was cooled to RT with 125 K min^{-1} . The SEM-BSE micrographs for the three annealing times are shown in images (b–d). Whereas annealing for 5 min leads to a pronounced formation of banded γ -grains after the aging step, 30 min annealing time lowered the amount of γ -grains precipitating within the colonies considerably. One hour was sufficient to lead to precipitation along the colony boundaries, coarsening up γ -lamellae.

leads to almost complete massive transformation,^[71,74] or the TNM alloy, where AC from a β -single-phase field region would be an option, which would not induce crack formation. As such, designing different alloys with a smaller resistivity to the formation of metastable TiAl microstructures favoring homogenization of inhomogeneous microstructures after EBM processing might be a possible way to minimize anisotropic mechanical properties and a low ductility, especially when EBM process parameters, that do generate homogeneous microstructures, are not applicable, for example, when technological limitations are present.

7. Conclusion

An extensive process parameter study on EBM Ti-48Al-2Cr-2Nb was performed to investigate the formation mechanism of banded microstructures, the solidification behavior as a function of the process parameters, the response to the long-term intrinsic annealing taking the microstructural evolution at the very top into account, and, finally, the microstructural response

to heat treatments as a matter of process-related history and remedial action involving a subsequent homogenization heat treatment. SEM, EPMA, EBSD, TMA, micro- as well as macro-hardness measurements, thermodynamic equilibrium calculations, numerical simulations, and XRD as well as heat treatment studies were utilized to obtain the results summarized as follows: 1) Going hand in hand with the overall Al loss, process-related heterogeneous Al distribution is the reason for the formation of banded microstructures due to the long-term intrinsic annealing during EBM at the building temperature. The overall chemistry (and, therefore, position in the phase diagram), phase fractions, macroscopic hardness, and $T_{\alpha T}$ change with an increase in energy input in accordance with the loss of Al. Numerical simulation has shown, that different processing parameters lead to different holding times in the liquid state, different maximum temperatures as well as melt pool sizes, and a number of remelting events, which highly influences the Al evaporation. 2) The response to the long-term intrinsic annealing is a matter of Al distribution due to Al evaporation during solidification, as α_2 preferably dissolves in non-Al-depleted areas, leading to grain growth of globular γ -phase. In case of extended chemical

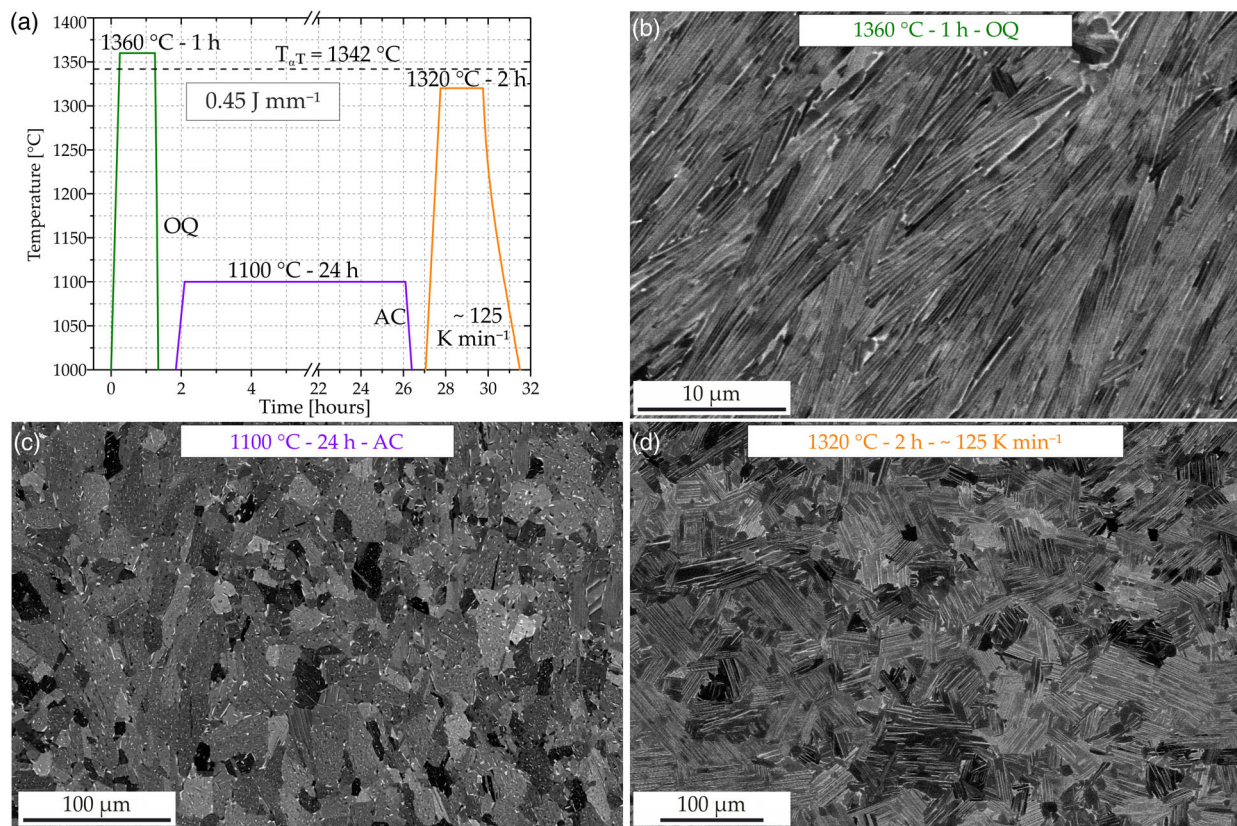


Figure 14. Designed homogenization heat treatment route involving a metastable phase transformation. The heat treatment is illustrated in (a). After a homogenization annealing in the α -single-phase field region at 1360 °C for 1 h followed by OQ the specimen was annealed at 1100 °C for 24 h to induce recrystallization. Lastly, the sample was annealed at 1320 °C for 2 h and finished with cooling to RT with 125 K min⁻¹. The microstructure consisting of γ_F after the OQ is shown in (b) and the near- γ microstructure after the annealing at 1100 °C is illustrated in (c). An exemplary duplex microstructure after the final annealing step is shown in (d).

heterogeneity of Al, coupled with a high loss of this element, α_2 is gathered in Al-depleted regions and inhibits grain growth of the γ -phase by Zener pinning. 3) The reason why the formation of banded microstructures is reported in the Al-rich EBM Ti-48Al-2Cr-2Nb is the fact that the thermodynamic equilibrium at the building temperature is rich in a single phase, with γ -TiAl being >90 vol%, enabling abnormal grain growth during the long-term intrinsic annealing. We did not report a similar microstructure for Al-lean TiAl alloys in a previous study, for example, the TNM alloy (Ti-43.5Al-4Nb-1Mo-0.1B), as they prohibit a different phase equilibrium at the building temperature.^[43] Inhomogeneous phase distributions were still witnessed due to preferential dissolution during the long-term intrinsic annealing in Al-depleted and non-Al-depleted regions. 4) Large γ -grain bands form on the bottom of the original melt pools, whereas duplex regions of γ and α_2 appear toward the top, where also the Al-depletion is reported, as lack of fusion porosity appears solely below these γ -bands. 5) Microstructures on the top are fully or nearly lamellar and undergo long-term intrinsic annealing when additional layers are built upon. Whether α_2 dissolves homogeneously or not is a matter of the heterogeneity of Al after consolidation, and may lead to the aforementioned abnormal grain growth, contrary to microstructure-global coarsening of γ -TiAl to

form homogeneous near- γ microstructures. 6) It is proposed that the non-equilibrium solidification during EBM for Ti-48Al-2Cr-2Nb happens via the α -phase due to the high solidification rates and cooling rates, which were calculated for the present process parameters by numerical simulation. Furthermore, thermodynamic equilibrium calculations revealed, that the $T_{0,L \rightarrow \alpha}$ is higher than $T_{0,L \rightarrow \beta}$ for Ti-48Al-2Cr-2Nb. With increasing energy input the solidification happens preferably along with the [0001] direction of α leading to an alignment of the {111} $_{\gamma}$ planes with the building direction on the top of the samples in accordance with the Blackburn orientation relationship. 7) Banded microstructures of Ti-48Al-2Cr-2Nb may react heterogeneously to heat treatments with the formation of γ/α_2 -colony bands during annealing in the $\alpha + \gamma$ two-phase field region to obtain a duplex or nearly lamellar microstructure. The reason is the abnormal growth of α -grains during the annealing in Al-depleted regions, forming large γ/α_2 -colonies on cooling. 8) The heterogeneous Al distribution can be homogenized by annealing in the α -single-phase field region. Subsequent oil quenching formed a microstructure of feathery γ (γ_F), which could be transformed into a homogeneous near- γ microstructure by subsequent annealing at 1100 °C for 24 h. Ensuing heat treatments provide a homogeneous microstructure without banded

features. 9) As oil quenching might induce cracks and metastable phase transformations, which are not suitable in industrial application, especially for large components, it is advisable to utilize process parameters with low energy inputs, which inhibit the formation of banded microstructures, but it must be ensured that microstructures are free of lack of fusion porosity. Alternatively, TiAl alloys providing the possibility for homogenization treatments on intermediate cooling rates, such as air cooling, might be suitable, for example, the TNM alloy or high Nb-bearing TiAl alloys. 10) Improved understanding of the process parameter- and the scan strategy-microstructure relationship in electron beam melted Ti-48Al-2Cr-2Nb alloy through process simulation and experimental data enables the possibility to build a solid knowledge pool of data. The data could be used then to train machine learning algorithms that, operating on machine hardware and software, may realize the full control of the process. This kind of adaptive control, apart from avoiding inhomogeneous microstructures, could allow adapting the process for obtaining locally tailored microstructures as a function of the mechanical requirements required on the local component section.

8. Experimental Section

Five different cubic samples with a size of $30 \times 30 \times 30 \text{ mm}^3$ with a nominal chemical composition of Ti-48Al-2Cr-2Nb were manufactured utilizing an Arcam A2X EBM machine (Arcam AB, Sweden) operating at an acceleration voltage U of 60 kV. The feedstock powder with the chemical composition of Ti-49.06Al-1.88Cr-1.98Nb and particle size ranging from 40 to $150 \mu\text{m}$ was also obtained from Arcam and produced by vacuum induction melting and inert gas atomization. Further information on the procedure of manufacturing TiAl powders by gas atomization can be found in related literature.^[75] The start plate preheating temperature was set to 1100°C , whereas the preheating temperature of the powder bed was set to 1050°C and the powder layer thickness to $90 \mu\text{m}$. A hatching mode, a meander-like pattern scan strategy, was used to selectively melt powder in the defined areas. A constant line offset l_{off} equal to $200 \mu\text{m}$ was used for this work in addition to rotating the beam direction by 90° every consecutive layer. Each respective set of manufacturing parameters, ν , I , and, subsequently, the calculated E_L and E_A , are presented in Table 4. As l_{off} was kept constant E_L and E_A represent the same general concept, and, therefore, E_L was chosen representatively for both terms in this article. As discussed in Section 1, the EBM process itself is not controlled by E_L at all, but it is suitable to describe the energy input for specimens with square melting area qualitatively, as it remains constant during the process. The respective E_L is, therefore, inserted in the micrographs. Process parameters were, furthermore, chosen in such a way that the expected changes in chemical composition due to evaporation stay at least partially within the controllable and applicable area, as TiAl components have to fulfill strict regulations as materials for the aeronautical application. Furthermore, the temperature profile recorded by the thermocouple placed below the building plate during the process is illustrated in Figure 15. As the recorded

Table 4. Processing parameters for EBM of the five investigated specimens, which are designated from A to E.

Sample designation	ν [mm s^{-1}]	I [mA]	E_L [J mm^{-1}]	E_A [J mm^{-2}]
A	2800	8	0.17	0.86
B	2800	10	0.21	1.07
C	2200	10	0.27	1.36
D	1600	10	0.38	1.88
E	1600	12	0.45	2.25

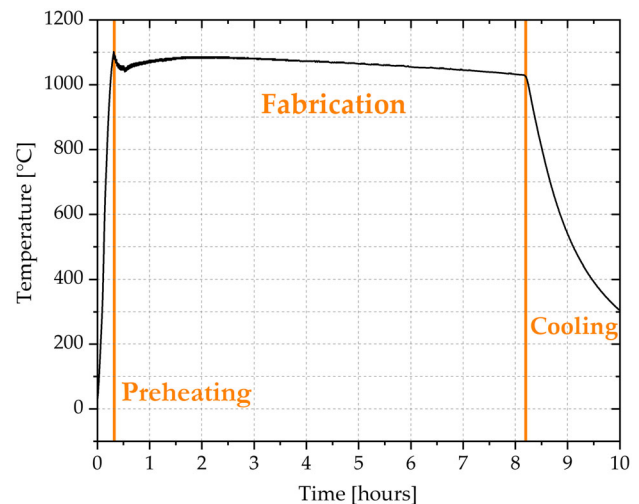


Figure 15. Temperature profile of the performed building job in $^\circ\text{C}$. The start plate preheating temperature was set to 1100°C ; the job took around 8 h. The subsequent cooling to RT was assisted by additional He.

thermal history shows, the job itself can be divided into a preheating step, ensuring that a predefined temperature is obtained on the start plate before starting the process, followed by fabricating the samples and a subsequent cooling assisted by additional He. Regarding the building process of the specimen or component, it is well known that each subsequent layer undergoes a separate preheating of the new powder layer followed by the selective melting of the powder based on the specimen geometry. Subsequently, post-heating is performed to balance the heat loss during melting and then the process repeats itself with lowering the building platform and the deposition of a new powder layer corresponding to the layer thickness, its preheating, and so on until the end of the process. The target was to investigate the last layer of the specimens in their unaltered state directly after melting and solidifying, so no post-heating was performed after the last melting step of the process.

XRF and CGHE (for oxygen) were used for chemical analysis; the results are presented in Table 1. The oxygen content ranged from 920 m ppm for sample E to 1000 m ppm for sample A and was, therefore, below the threshold level when interstitial impurity significantly reduces the ductility of the TiAl alloy.^[7] The porosity was analyzed by image analysis on polished specimens with the software ImageJ obtained via a visible light microscope DM ILM5000 by Leica, Germany. The specimens were separated parallel to the building direction, grounded, and electrolytically polished using a Struers Lectropol, Germany according to the previous study.^[76] Microstructures were visualized via SEM using a field emission gun dual focused ion beam device Versa 3D Dual Beam from FEI, USA in BSE mode operating at 10 kV acceleration voltage. The building direction Z is upwards for all micrographs shown in this article. Single scale bars always apply to all micrographs in the figures. Additionally, EBSD was performed to gain insights on phase morphology and solidification behavior using the aforementioned FEI system with a Hikari XP EBSD camera from EDAX, USA. Samples for EBSD analysis were subjected to an additional vibration-polishing step with a VibroMet 2 from Buehler, Germany, for 60 min with a colloidal silica suspension. Data collection were carried out via the software Team 4.3 and thereupon evaluated via TSL OIM Analysis 7, both from EDAX. As it is challenging for the EBSD technique to properly detect γ -TiAl as a tetragonal phase due to the c/a ratio being close to 1,^[77,78] γ -TiAl was measured as the cubic phase. The measurements were conducted at an acceleration voltage of 30 kV, a step size of 500–1000 nm, a spot size of 7, and a binning mode of the EBSD camera of 2×2 and 4×4 .

To protect the consolidated layers during sample preparation for EBSD a Mo thin film was deposited on the TiAl substrates. Prior to deposition,

the chamber was evacuated to a base pressure of less than 3×10^{-5} Pa. During plasma etching, a glow discharge with a discharge power of 0.8 kW and an Ar gas pressure of 0.32 Pa was generated. The Mo thin film with a thickness of around 10 μm was synthesized at a discharge power of 8 kW and an Ar working gas pressure of 0.53 Pa using an industrial-scale in-line DC magnetron sputter deposition system of type FHR.Line.600.V (FHR, Germany) equipped with a rotating cylindrical Mo target (ϕ 150 mm \times 600 mm). Information regarding the deposition process can be found in the related literature.^[79] Furthermore, substrate temperatures did not exceed 300 °C and it is, therefore, unexpected to alter any TiAl microstructure.

To perform quantitative phase analysis XRD measurements were performed on bulk material using Cu-K α radiation in an angular range of 11°–82° and a step size of 0.02° in Bragg–Brentano geometry using a D8 Advance diffractometer by Bruker AXS, Germany. The quantitative phase analysis was subsequently performed by Rietveld refinement based on the guidelines described in related literature^[80] using the software TOPAS 4.1 by Bruker.

Phase transformation temperatures were assessed by TMA via a Setaram Setsys Evolution, France, with a sample geometry of $5 \times 5 \times 10$ mm³ under an Ar flow of 20 ml min^{−1} to prevent oxidation and a heating rate of 5 K min^{−1} up to a temperature of 1400 °C. The correlation between the $T_{\alpha\beta}$ and the second peak of the derivative curve of the displacement as a function of temperature was already demonstrated by Terner et al.^[57]

To illustrate the chemical distribution of the elements EPMA was performed using a SuperProbe electron probe microanalyzer JXA-8200 from Jeol, Japan, operating at an acceleration voltage of 15 kV with a beam current of 10 nA, a spot diameter of 1 μm , and a dwell time of 30 ms. Pure elements served as standards.

Selected specimens were subjected to heat treatments under the atmospheric condition in a Carbolite RHF 1600 furnace by Carbolite Gero, Germany, equipped with type-S thermocouples to visualize the different responses to thermal treatments and explain the microstructural evolution.

To estimate the dependency of the mechanical properties from the process-related history, hardness measurements according to Vickers HV10 (testing force of 10 kp/98.07 N) and Vickers HV0.05 (testing force of 0.05 kp/0.49 N) were performed using a Qness Q60A+ microhardness tester by ATM Qness, Germany. Values for macroscopic hardness were established based on the arithmetic mean of 10 independent indentations. Microscopic hardness maps were generated with a size of $31 \times 31 = 961$ indents with 50 μm in between to get insights on the microscopic mechanical properties and the hardness distribution, which equals size of 1.5×1.5 mm². Special care was taken to prevent indentation of truncated pores as all investigated specimens were in their as-EBM state.

To gain information on the phase transformation pathway and phase equilibria as well as phase transformation temperatures thermodynamic equilibrium calculations based on the CALPHAD methodology were performed using Thermo-Calc 4.1 with a commercially available database for TiAl.^[81–83]

To get additional data on the effect of process parameters on the final microstructure and the final chemical composition of the material, numerical simulations were performed using the 3D FE thermal model developed by Galati et al.,^[84] This thermal model is specifically designed to simulate the EBM process at the melt pool scale. With respect to the literature, the modeling approach proposed by Galati et al.,^[84] was based on analytical models for the energy source and for the material properties of the powder bed that considered the peculiarity of EBM.

The energy source consisted of uniform heat flux with an intensity q calculated according to Equation (3)

$$q = \eta \frac{UI}{S} \quad (3)$$

where S is the cross-section of the beam. η is a corrective parameter that couples the actual electron distribution with the uniform heat source and can be calculated by numerical integration of Equation (4)

$$\eta = \int_{\Gamma} \frac{1}{2\pi\sigma^2} \exp\left(-\frac{(x_1 - x_{10})^2 - (x_2 - x_{20})^2}{2\sigma^2}\right) d\Gamma \quad (4)$$

where x_1 and x_2 are the generic Cartesian coordinates, and x_{10} and x_{20} are the coordinates of the starting point of the center of the focal spot of the electron beam (EB). σ is the standard deviation of the effective beam diameter D_E that assesses the lateral spread of the EB when it impacts the powder surface. This diameter is obtained by simulating the electron trajectories numerically via the Monte Carlo method. The material, including the powder, is modeled as a continuum, in which the thermal conductivity depends on the average size of the particles, the powder bed porosity, and the corresponding temperature-dependent bulk material properties. The porosity of the powder bed, ϕ , was assumed to be 0.68. The temperature-dependent thermal diffusivity for the bulk material has been measured by laser flash measurements from 300 to 1000 °C, while the corresponding thermal conductivity was calculated from the thermal diffusivity, the specific heat capacity, and the density, as reported in the previous study^[85] for higher temperatures in the solid and molten states. The specific heat and the latent heat of fusion of the powder bed were assumed to be equal to those of the solid bulk material and they were also collected from the previous study.^[85]

The simulation domain consisted of two regions: a single layer of powder material on a substrate of solid bulk material. 2D shell elements were used to decrease the calculation time.^[86] The thickness of the shell elements was set to 10 mm for the bulk substrate and 0.090 mm (equal to the layer thickness) for the powder layer. The different regions were fused together by a tie constraint.^[87] On the powder bed region, a fine element size equal to 0.050 mm was used. The overall dimensions of the simulation domain are 30×30 mm². For each node of the powder domain, a variable called MAT_ID was defined to record the state of the material. The material state was defined as “powder” (MAT_ID = 0) before the melting and as “bulk” (MAT_ID = 1) after the melting. The bulk material state (MAT_ID = 1) was used for both the liquid and solid states. The material properties were, therefore, updated from powder to bulk according to the material state variable MAT_ID. The use of MAT_ID allowed to account for the correct heat transfer into and between the powder and the melted and solidified material. For a detailed description, please see previous studies.^[84,88]

The initial temperature for the whole domain was set equal to the pre-heating temperature. The same temperature was used for the adiabatic boundary conditions on all surfaces except the top surface, where a local thermal load according to the energy source model was applied. The melting of the entire layer was simulated by moving the thermal load with a constant speed parallel to one side of the domain. When the entire length is melted the thermal load is repositioned to the starting point and translated perpendicularly to the melted line of a certain distance corresponding to the line offset. A subsequent movement of the thermal load parallel to the previous melted line emulates the hatching strategy. The process is repeated until the entire domain of the powder region has been scanned. Further details about the numerical modeling of the hatching strategy are available in a previous study.^[89] The model was implemented in Abaqus/Standard. The thermal energy balance problem was solved as a function of both space and time. A thermal energy density is considered the latent enthalpy influence during melting. When the temperature drops between the liquidus temperature (T_{Liquidus}) and T_{Solidus} the liquid fraction determines how much of the latent heat of fusion is going to be included in the enthalpy calculation. The liquid fraction was determined by interpolation between the T_{Liquidus} and T_{Solidus} temperatures. In accordance with the experimental process parameters (Table 4), the inputs for the simulation are listed in Table 5.

The simulations were run using a computer equipped with an Intel® Core™ i7-6700K 4.00 GHz, RAM 32 GB. From numerical results, the thermal history of the material and the melt pool dimensions have been extracted for each sample. These results have been collected at the center of the domain to have stable conditions. The holding time of the material in the liquid state, the cooling rate, and the solidification rates have been calculated numerically.

Table 5. Input parameters for the numerical simulation of the EBM process with the sample designation, the scan speed ν , the corrective parameter η , and the heat flux.

Sample designation	ν [mm s ⁻¹]	η	Heat flux [W mm ⁻²]
A	2800	0.41	790
B	2800	0.30	828
C	2200	0.41	790
D	1600	0.41	790
E	1600	0.47	796

Acknowledgements

This project has received funding from the Clean Sky 2 Joint Undertaking under the European Union's Horizon 2020 research and innovation program under grant agreement No. 821274. The Integrated Additive Manufacturing Centre at Politecnico di Torino (IAM@PoliTo), where the specimens were produced, is acknowledged. Furthermore, thanks to Sabrina Hirn for the thin film deposition and Melissa Allen for the chemical analysis.

Conflict of Interest

The authors declare no conflict of interest.

Data Availability Statement

Research data are not shared.

Keywords

additive manufacturing, phase diagram, simulation, texture, titanium aluminides

Received: September 7, 2021

Revised: October 11, 2021

Published online: November 10, 2021

- [1] F. Calignano, D. Manfredi, E. P. Ambrosio, S. Biamino, M. Lombardi, E. Atzeni, A. Salmi, P. Minetola, L. Iuliano, P. Fino, *Proc. IEEE* **2017**, 105, 593.
- [2] W. E. Frazier, *J. Mater. Eng. Perform.* **2014**, 23, 1917.
- [3] G. Baudana, S. Biamino, D. Ugues, M. Lombardi, P. Fino, M. Pavese, C. Badini, *Met. Powder Rep.* **2016**, 71, 193.
- [4] M. Galati, L. Iuliano, *Addit. Manuf.* **2018**, 19, 1.
- [5] D. M. Dimiduk, *Mater. Sci. Eng., A* **1999**, 263, 281.
- [6] A. Lasalmonie, *Intermetallics* **2006**, 14, 1123.
- [7] Y.-W. Kim, D. M. Dimiduk, *JOM* **1991**, 43, 40.
- [8] H. Clemens, S. Mayer, *Adv. Eng. Mater.* **2013**, 15, 191.
- [9] S. Mayer, P. Erdely, F. D. Fischer, D. Holec, M. Kastenhuber, T. Klein, H. Clemens, *Adv. Eng. Mater.* **2017**, 19, 1600735.
- [10] Intergovernmental Panel on Climate Change (IPCC), in *Aviation and the Global Atmosphere* (Eds.: J. E. Penner, D. H. Lister, D. J. Griggs, D. J. Dokken, M. McFarland), Cambridge University Press, Cambridge, UK **1999**.
- [11] V. Güther, M. Allen, J. Klose, H. Clemens, *Intermetallics* **2018**, 103, 12.
- [12] X. Wu, *Intermetallics* **2006**, 14, 1114.
- [13] V. Bojarevics, K. Pericleous, R. A. Harding, M. Wickins, *Metall. Mater. Trans. B* **2004**, 35, 785.
- [14] S.-C. Huang, US 4789092, General Electric Company, **1989**.
- [15] B. P. Bewlay, M. Weimer, T. Kelly, A. Suzuki, P. R. Subramanian, *Mater. Res. Soc. Symp. Proc.* **2013**, 1516, 49.
- [16] P. Bartolotta, J. Barrett, T. Kelly, R. Smashey, *JOM* **1997**, 49, 48.
- [17] T. Tetsui, K. Shindo, S. Kobayashi, M. Takeyama, *Scr. Mater.* **2002**, 47, 399.
- [18] G. Baudana, S. Biamino, B. Klöden, A. Kirchner, T. Weißgärber, B. Kieback, M. Pavese, D. Ugues, P. Fino, C. Badini, *Intermetallics* **2016**, 73, 43.
- [19] C. Körner, *Int. Mater. Rev.* **2016**, 61, 361.
- [20] B. P. Bewlay, S. Nag, A. Suzuki, M. J. Weimer, *Mater. High Temp.* **2016**, 33, 549.
- [21] L. Löber, S. Biamino, U. Ackelid, S. Sabbadini, P. Epicoco, P. Fino, J. Eckert, *Solid Freeform Fabrication Symp. Proc.* **2011**, 547.
- [22] S. Biamino, A. Penna, U. Ackelid, S. Sabbadini, O. Tassa, P. Fino, M. Pavese, P. Gennaro, C. Badini, *Intermetallics* **2011**, 19, 776.
- [23] Y. Chen, H. Yue, X. Wang, *Mater. Sci. Eng., A* **2018**, 713, 195.
- [24] Y. Chen, H. Yue, X. Wang, S. Xiao, F. Kong, X. Cheng, H. Peng, *Mater. Charact.* **2018**, 142, 584.
- [25] K. Cho, R. Kobayashi, J. Y. Oh, H. Y. Yasuda, M. Todai, T. Nakano, A. Ikeda, M. Ueda, M. Takeyama, *Intermetallics* **2018**, 95, 1.
- [26] D. Cormier, O. Harrysson, T. Mahale, H. West, R. Vilar, *Res. Lett. Mater. Sci.* **2007**, 2007, 34737.
- [27] M. Todai, T. Nakano, T. Liu, H. Y. Yasuda, K. Hagihara, K. Cho, M. Ueda, M. Takeyama, *Addit. Manuf.* **2017**, 13, 61.
- [28] L. E. Murr, S. M. Gaytan, A. Ceylan, E. Martinez, J. L. Martinez, D. H. Hernandez, B. I. Machado, D. A. Ramirez, F. Medina, S. Collins, R. B. Wicker, *Acta Mater.* **2010**, 58, 1887.
- [29] A. Mohammad, A. M. Alahmari, K. Moiduddin, M. K. Mohammed, A. Alomar, R. K. Renganayagalu, *Metals* **2016**, 6, 25.
- [30] A. Mohammad, A. M. Alahmari, M. K. Mohammed, R. K. Renganayagalu, K. Moiduddin, *Materials* **2017**, 10, 211.
- [31] A. Mohammad, A. M. Al-Ahmari, V. K. Balla, M. Das, S. Datta, D. Yadav, G. D. Janaki Ram, *Mater. Des.* **2017**, 133, 186.
- [32] J. Wang, K. Yang, N. Liu, L. Jia, G. Y. Yang, H. P. Tang, *JOM* **2017**, 69, 2751.
- [33] H. Yue, Y. Chen, X. Wang, F. Kong, *J. Alloys Compd.* **2018**, 750, 617.
- [34] A. Klassen, V. E. Forster, V. Juechter, C. Körner, *J. Mater. Process. Technol.* **2017**, 247, 280.
- [35] Y.-K. Kim, S.-J. Youn, S.-W. Kim, J. Hong, K.-A. Lee, *Mater. Sci. Eng., A* **2019**, 763, 138138.
- [36] J. Schwerdtfeger, C. Körner, *Intermetallics* **2014**, 49, 29.
- [37] M. Seifi, A. A. Salem, D. P. Satko, U. Ackelid, S. L. Semiatin, J. J. Lewandowski, *J. Alloys Compd.* **2017**, 729, 1118.
- [38] V. Tebaldo, M. G. Faga, *J. Mater. Process. Technol.* **2017**, 244, 289.
- [39] E. Cakmak, P. Nandwana, D. Shin, Y. Yamamoto, M. N. Gussev, I. Sen, M. H. Seren, T. R. Watkins, J. A. Haynes, *Materialia* **2019**, 6, 100284.
- [40] M. Jop, R. Wartbichler, P. Staron, E. Maawad, S. Mayer, H. Clemens, *Pract. Metallogr.* **2020**, 57, 84.
- [41] S.-J. Youn, Y.-K. Kim, S.-W. Kim, K.-A. Lee, *Intermetallics* **2020**, 124, 106859.
- [42] B. Lin, W. Chen, Y. Yang, F. Wu, Z. Li, *J. Alloys Compd.* **2020**, 830, 154684.
- [43] R. Wartbichler, H. Clemens, S. Mayer, *Adv. Eng. Mater.* **2019**, 21, 1900800.
- [44] R. Wartbichler, R. Bürstmayr, H. Clemens, S. Mayer, *Pract. Metallogr.* **2019**, 56, 220.
- [45] P. L. Narayana, C.-L. Li, S.-W. Kim, S.-E. Kim, A. Marquardt, C. Leyens, N. S. Reddy, J.-T. Yeom, J.-K. Hong, *Mater. Sci. Eng., A* **2019**, 756, 41.

- [46] M. Terner, S. Biamino, P. Epicoco, A. Penna, O. Hedin, S. Sabbadini, P. Fino, M. Pavese, U. Ackelid, P. Gennaro, F. Pelissero, C. Badini, *Steel Res. Int.* **2012**, 83, 943.
- [47] H. P. Tang, G. Y. Yang, W. P. Jia, W. W. He, S. L. Lu, M. Qian, *Mater. Sci. Eng., A* **2015**, 636, 103.
- [48] W. Kan, Y. Liang, H. Peng, B. Chen, H. Guo, J. Lin, *JOM* **2017**, 69, 2596.
- [49] W. Kan, B. Chen, C. Jin, H. Peng, J. Lin, *Mater. Des.* **2018**, 160, 611.
- [50] W. Kan, B. Chen, H. Peng, Y. Liang, J. Lin, *J. Alloys Compd.* **2019**, 809, 151673.
- [51] V. Juechter, M. M. Franke, T. Merenda, A. Stich, C. Körner, R. F. Singer, *Addit. Manuf.* **2018**, 22, 118.
- [52] M. Terner, S. Biamino, P. Epicoco, A. Penna, O. Hedin, S. Sabbadini, P. Fino, M. Pavese, U. Ackelid, P. Gennaro, F. Pelissero, C. Badini, *Steel Res. Int.* **2012**, 83, 943.
- [53] E. O. Hall, *Proc. Phys. Soc. B* **1951**, 64, 747.
- [54] Y. Li, A. J. Bushby, D. J. Dunstan, *Proc. R. Soc. A* **2016**, 472, 20150890.
- [55] M. Schloffer, F. Iqbal, H. Gabrisch, E. Schwaighofer, F.-P. Schimansky, S. Mayer, A. Stark, T. Lippmann, M. Göken, F. Pyczak, H. Clemens, *Intermetallics* **2012**, 22, 231.
- [56] L. Spieß, G. Teichert, R. Schwarzer, H. Behnken, C. Genzel, *Moderne Röntgenbeugung: Röntgendiffraktometrie für Materialwissenschaftler, Physiker und Chemiker*, Vieweg + Teubner Verlag/GWV Fachverlage GmbH, Wiesbaden, Germany **2009**.
- [57] M. Terner, S. Biamino, D. Ugues, S. Sabbadini, P. Fino, M. Pavese, C. Badini, *Intermetallics* **2013**, 37, 7.
- [58] D. A. Porter, K. E. Easterling, M. Y. Sherif, *Phase Transformations in Metals and Alloys*, CRC Press, Boca Raton, FL **2009**.
- [59] C. S. Smith, *Trans. AIME* **1948**, 175, 15.
- [60] K. Huang, R. E. Logé, in *Reference Module in Materials Science and Materials Engineering* (Ed.: H. Saleem), Elsevier, Amsterdam **2016**.
- [61] M. Hillert, *Acta Metall.* **1965**, 13, 227.
- [62] G. Gottstein, *Physical Foundations of Materials Science*, Springer-Verlag, Berlin Heidelberg, Germany **2004**.
- [63] M. J. Blackburn, in *The Science, Technology and Application of Titanium* (Eds.: R. I. Jaffee, N. E. Promisel), Pergamon Press Ltd. Oxford, UK **1970**, p. 633.
- [64] M. Yamaguchi, D. R. Johnson, H. N. Lee, H. Inui, *Intermetallics* **2000**, 8, 511.
- [65] H. E. Helmer, C. Körner, R. F. Singer, *J. Mater. Res.* **2014**, 29, 1987.
- [66] M. Charpentier, D. Daloz, A. Hazotte, E. Gautier, G. Lesoult, M. Grange, *Metall. Mater. Trans. A* **2003**, 34A, 2139.
- [67] C. Kenel, D. Grolimund, J. L. Fife, V. A. Samson, S. van Petegem, H. van Swygenhoven, C. Leinenbach, *Scr. Mater.* **2016**, 114, 117.
- [68] S. S. Al-Bermani, M. L. Blackmore, W. Zhang, I. Todd, *Metall. Mater. Trans. A* **2010**, 41, 3422.
- [69] J. Liu, P. Staron, S. Riekehr, A. Stark, N. Schell, N. Huber, A. Schreyer, M. Müller, N. Kashaev, *Intermetallics* **2015**, 62, 27.
- [70] F. Appel, U. Brossmann, U. Christoph, S. Eggert, P. Janscheck, U. Lorenz, J. Müllauer, M. Oehring, J. D. H. Paul, *Adv. Eng. Mater.* **2000**, 2, 699.
- [71] H. Clemens, A. Bartels, S. Bystrzanowski, H. Chladil, H. Leitner, G. Dehm, R. Gerling, F. P. Schimansky, *Intermetallics* **2006**, 14, 1380.
- [72] P. Wang, G. B. Viswanathan, V. K. Vasudevan, *Metall. Trans. A* **1992**, 23A, 690.
- [73] S. R. Dey, E. Bouzy, A. Hazotte, *Acta Mater.* **2008**, 56, 2051.
- [74] J. Lapin, T. Pelachová, M. Dománková, *Intermetallics* **2011**, 19, 814.
- [75] R. Gerling, H. Clemens, F. P. Schimansky, *Adv. Eng. Mater.* **2004**, 6, 23.
- [76] M. Schloffer, T. Schmoelzer, S. Mayer, E. Schwaighofer, G. Hawranek, F.-P. Schimansky, F. Pyczak, H. Clemens, *Pract. Metallogr.* **2011**, 48, 594.
- [77] L. Germain, S. R. Dey, M. Humbert, N. Gey, *J. Microsc.* **2007**, 227, 284.
- [78] S. R. Dey, E. Bouzy, A. Hazotte, *Intermetallics* **2006**, 14, 444.
- [79] T. Jörg, M. J. Cordill, R. Franz, O. Glushko, J. Winkler, C. Mitterer, *Thin Solid Films* **2016**, 606, 45.
- [80] L. B. McCusker, R. B. von Dreele, D. E. Cox, D. Louer, P. Scardi, *J. Appl. Crystallogr.* **1999**, 32, 36.
- [81] J.-O. Andersson, T. Helander, L. Höglund, P. Shi, B. Sundman, *Calphad* **2002**, 26, 273.
- [82] N. Saunders, in *Gamma Titanium Aluminides* (Eds.: Y.-W. Kim, D. M. Dimiduk, M. H. Loretto), TMS, Warrendale, PA **1999**, p. 183.
- [83] N. Saunders, A. P. Miodownik, *CALPHAD (Calculation of Phase Diagrams): A Comprehensive Guide*, Pergamon Press, London, UK **1998**.
- [84] M. Galati, L. Iuliano, A. Salmi, E. Atzeni, *Addit. Manuf.* **2017**, 14, 49.
- [85] C. Cagran, B. Wilthan, G. Pottlacher, B. Roebuck, M. Wickins, R. A. Harding, *Intermetallics* **2003**, 11, 1327.
- [86] M. Galati, A. Snis, L. Iuliano, *Addit. Manuf.* **2019**, 30, 100897.
- [87] Dassault Systèmes, *Abaqus*, ABAQUS Documentation, Providence, RI **2014**.
- [88] M. Galati, A. Snis, L. Iuliano, *Comput. Math. Appl.* **2019**, 78, 2417.
- [89] M. Galati, O. Di Mauro, L. Iuliano, *Crystals* **2020**, 10, 532.